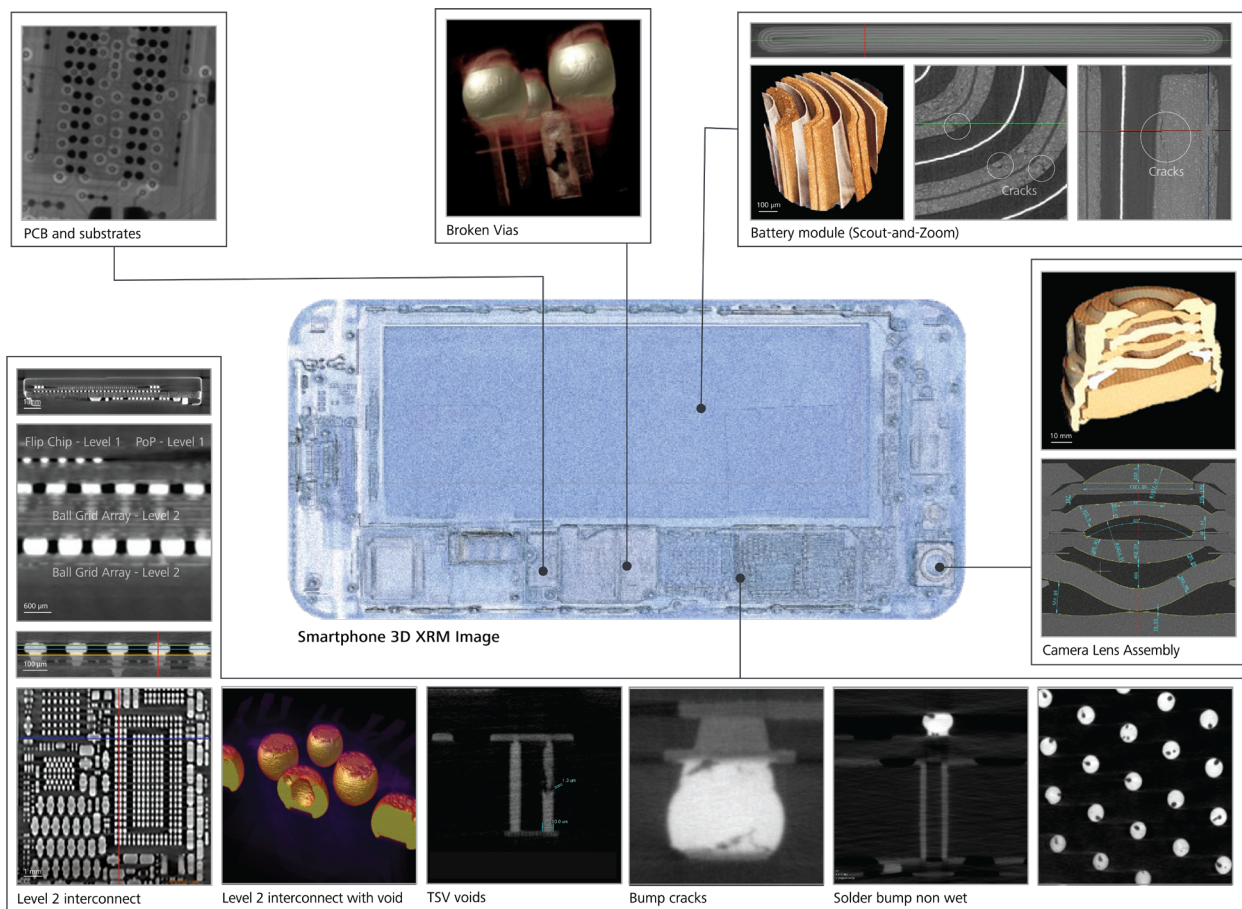


Non-destructive Failure Analysis with ZEISS X-ray Microscopy



Seeing beyond

Introduction

Non-destructive imaging of semiconductor packages has become routine in failure analysis (FA). ZEISS Xradia Versa family of 3D X-ray microscopes are widely adopted across the industry for non-destructive FA of advanced packages that surpasses conventional 2D X-ray and CT tools and minimizing the need for traditional physical cross-sectioning for package analysis.

The content in this compendium comprises some of the early articles highlighting the ZEISS Xradia Versa for advancing non-destructive failure analysis techniques in semiconductor packaging and use cases highlighting the superior resolution and 3D x-ray imaging capabilities. The recent publications included also introduce and explore innovations in AI and deep learning techniques for 3D reconstruction workflows that enhance SNR, throughput and recover high resolution in 3D X-ray imaging that accelerates semiconductor package failure analysis.

3D X-ray Microscopy: A Non-destructive High Resolution Imaging Technology that Replaces Physical Cross-sectioning for 3DIC Packaging	3
Non-destructive 3D X-ray Imaging for Advanced Packaging Failure Analysis	12
A Breakthrough in Resolution and Scan Speed: Overcome the Challenges of 3D X-ray Imaging Workflows for Electronics Package Failure Analysis	17
Accelerate Your 3D X-ray Failure Analysis by Deep Learning High Resolution Reconstruction	22
A Deep Learning Reconstruction Technique and Workflow to Enhance 3D X-ray Imaging Resolution and Speed for Electronics Package Failure Analysis	27

3D X-ray Microscopy: A Non-destructive High Resolution Imaging Technology that Replaces Physical Cross-sectioning for 3DIC Packaging

Bruce Johnson et al., 2013
Carl Zeiss X-ray Microscopy, Ltd.

Tulip Chou, Y.L. Kuo
Taiwan Semiconductor Manufacturing Company, Ltd.

Abstract

In this paper, we describe the novel technique of using leading edge X-ray microscopy (XRM) technology to replace physical cross-sectioning in failure analysis (FA) and 3-dimensional integrated circuit (3DIC) process development. Contrary to general consensus that 3D X-ray is too slow, we explain how XRM can be used to obtain high quality cross-section images within 5-300 minutes per measurement depending on the physical properties (materials, feature sizes, and outer dimensions) of the sample and the minimum tolerable image quality needed to visualize a defect. The specifics of the inspection technique itself and how X-rays interact with the sample to achieve high-quality images will be discussed and contrasted with conventional 3D micro computed tomography (MicroCT) technology. Furthermore, understanding the effects that imaging parameters, such as voltage, power, exposure time, resolution, number of projections, etc, have in the quality of an image, can help the user reduce the 3D X-ray inspection time considerably. A TSMC test vehicle package is used to illustrate the effects of inspection time in image quality, and to compare and contrast the quality of an optical image taken from a physical cross-section and a virtual cross-section image taken from an XRM tomography.

Introduction

2D X-ray and conventional MicroCT technologies used in the development of ball grid array, thermal compression bonding, and flip chip technologies cannot be extended to provide the image quality needed for the development of 3DIC packages. While the resolution provided by these techniques is useful to image large voids, rough misalignments, and non-contact opens from top-views of first- and second-level interconnects, conventional X-ray techniques quickly become inadequate as more layers with smaller feature sizes are stacked on top of each other as it is in the case of multi-chip packages, interposers, and through-silicon vias [1]. Physical cross-sectioning is still the most widely used technique for 3DIC package development because the high quality (high resolution and high contrast) side-view images give enough detail to measure critical structures and defects. Despite these advantages, physical cross-sectioning is far from an optimal solution to address the increasing requirements of 3DIC packages because it is destructive and time consuming. In addition, stress relief produced by cross-sectioning may in fact obfuscate clues—by introducing debris or damaging soft layers—about the original root cause of the defect of interest.

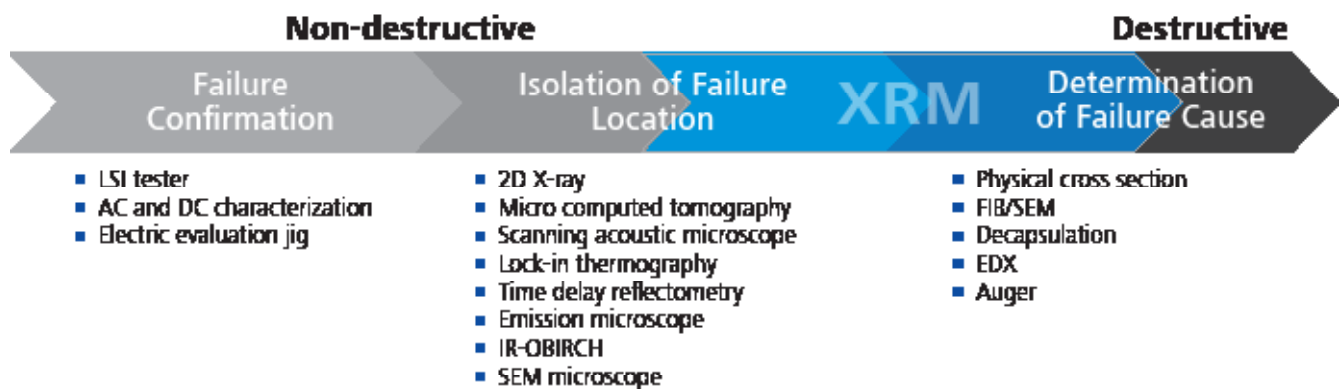


Figure 1 Proposed use of non-destructive X-ray microscopy (XRM) to improve the units per hour (UPH) of intact samples requiring inspection in the Failure Analysis Workflow and to shorten the time-to-market of 3DIC process development [3]. The traditional non-destructive techniques found in most FA labs today are becoming unsuitable to address the increasingly complex multilayered architectures of 3DIC packages. X-ray radiography (which includes "2D X-ray" and "3D X-ray MicroCT") and scanning acoustic microscope have been the standard non-destructive techniques for locating and identifying failure causes. However, the resolution that they deliver is no longer able to meet the requirements of advanced packages, forcing users to resort to destructive techniques.

Furthermore, defects can be completely missed if the incorrect polishing orientation is chosen. XRM, a powerful 3D X-ray variant technique, has demonstrated success in replacing physical cross-sections in FA labs and shows great potential to bridge the gaps in 3DIC production metrology [1,2]. Unlike 2D X-ray and conventional MicroCT techniques that rely exclusively in geometric magnification with low signal-to-noise flat panel detectors, XRM employs geometric and optical image magnification to achieve higher spatial resolution, even for large package sizes. In this way XRM is being used to collect high-quality non-destructive images that are comparable in quality to the ones obtained from scanning electron microscope (SEM) and optical micrographs, enabling an unparalleled imaging capability to the FA and process development workflows (see Figure 1) [3].

Recent advances in XRM obtain near-SEM quality images with reasonable data collection times. To appreciate the capabilities and limitations of this novel technique as it applies to 3DIC packaging, it is important to understand the differences between MicroCT and XRM techniques and the way X-rays interact with the sample in XRM to achieve high quality images.

MicroCT vs XRM

3D X-ray data is a virtual volumetric region in space that is reconstructed from many 2D X-ray projections passing through a sample as it rotates about an axis. The two most known 3D data collection techniques to the semiconductor industry are laminography and computed tomography (CT).

Despite being fast, laminography has physical limitations—2D projections are collected at higher incident angles, causing image artifacts—that fundamentally limit its ability to achieve high spatial resolution. CT, on the other hand, uses a filtered-back projection reconstruction technique to generate 3D virtual models of internal structures from 2D X-ray projections that are collected in small intervals over a range of angles, typically 180° or 360°. MicroCT was developed to achieve micrometer voxel (the 3D analog of a 2D pixel) resolution. However, this technique is subject to tradeoffs between sample size and achievable spatial resolution. The relationship can be modeled by (1),

$$d_{total} = \frac{\sqrt{r_D^2 + \left(S \frac{r_{od}}{r_{so}}\right)^2}}{M} \quad (1)$$

where d_{total} is the total spatial resolution, r_D is detector pixel size, S is X-ray spot size, M is geometric magnification, r_{so} is source-to-object distance, and r_{od} is object-to-detector distance, respectively and graphically represented in Figure 2 [2].

Furthermore, to maximize spatial resolution, MicroCT relies on maximizing geometric magnification, M , which is described by (2) below.

$$M = \frac{r_{od} + r_{so}}{r_{so}} \quad (2)$$

Thus, in order to maximize geometric magnification, the source-to-object distance must be made very small, limiting the working distance available for high-resolution analysis. As a result, high-resolution imaging of larger samples is not possible.

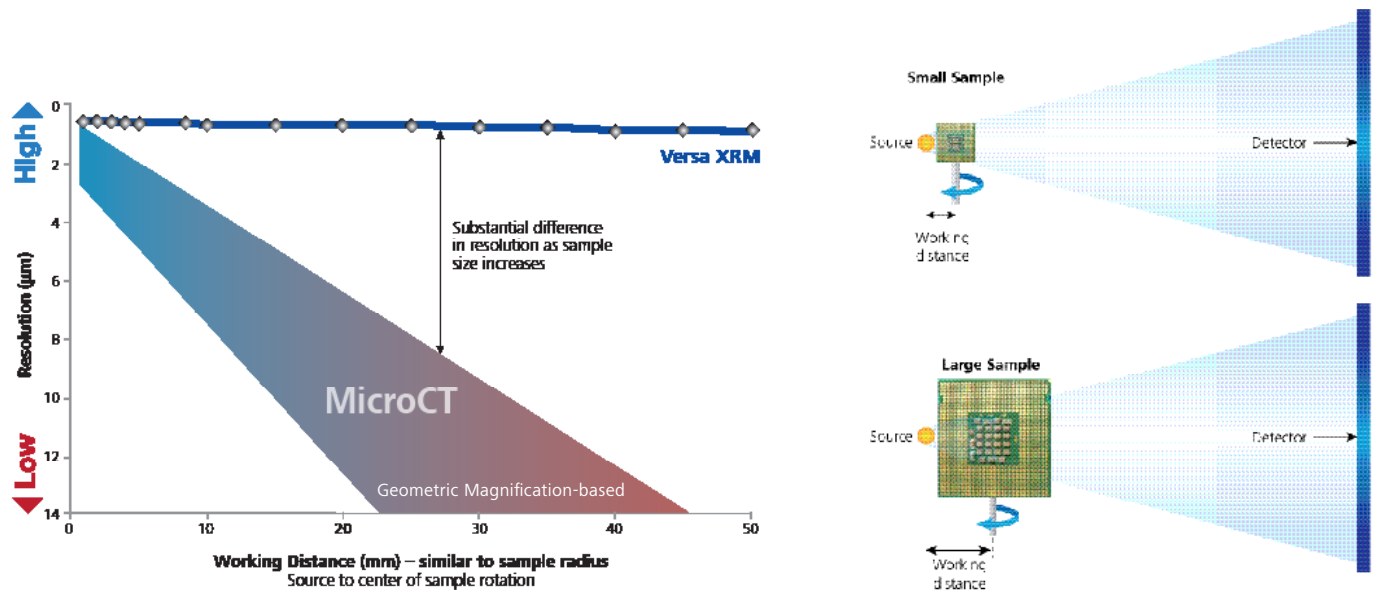


Figure 2 The red region shows the tradeoff between resolution and sample size in conventional MicroCT. The blue line shows “resolution-at-distance” achievable with XRM enhanced optics. The image on the right illustrates how geometric magnification is decreased in a full-angle CT scan as the sample size increases.

To improve on this limitation, MicroCT can continue to develop in three main ways:

a) Increase equipment footprint: This increases the sample-to-detector distance, thus achieving higher geometric magnification for larger samples. However, the impact of this leads not only to a larger equipment, but also degrades the image quality because having the source and detector so far apart reduces the signal-to-noise ratio of the image.

b) Reduce source spot size: The X-ray beam is generated by focusing an electron beam onto a target material (typically Tungsten or Diamond). In order to achieve a small spot size, high densities of energy need to be focused onto a very small region, where heat dissipation becomes an important challenge that can cause short filament lifetimes and/or unstable X-ray power output. Commercially available sources with spot sizes down to $\sim 0.25 \mu\text{m}$ are available, but they are limited to low power levels (2-5 W) only and thus lower energies (up to $\sim 90 \text{ kV}$). At this energy range (0-90 kV), the effective penetration of highly attenuating materials (as it is typical in materials found in 3DIC packages, like SAC305 solders, Cu, Au, fiber glass, etc.) is minimal, making these sources unsuitable for a wide range of semiconductor samples. In contrast, XRM does not rely on small source spot sizes to achieve high resolution, since magnification is mostly achieved by optical means as opposed to geometric means. For this reason, higher power sources can be used in these systems, allowing for higher voltages that can penetrate through denser materials. A typical X-ray source used in XRM equipment can achieve stable 10 W output at 150 kV with spot sizes of 1-3 μm and achieve higher spatial resolution than MicroCT with a source spot size of $0.25 \mu\text{m}$.

c) Reduce pixel size of flat panel detectors: Current detector technologies being used in X-ray systems include flat panel detectors and charge-coupled detectors (CCD). Flat panel detectors are able to obtain larger fields of view (FOV) at the expense of lower signal and larger pixel sizes (typically 200-300 μm) whereas CCDs offer smaller FOVs at a gain in quantum efficiency and pixel size (typically $\sim 35 \mu\text{m}$). Increasing the size of a flat panel detector (e.g. going from a 4 Mp to a 16 Mp) only increases the FOV and digital magnification, not spatial resolution. Digital magnification does not lead to better image detail; it only gives the ability to zoom-in further in the display screen.

XRM takes advantage of state-of-the-art detectors (optics with enhanced scintillators) developed for synchrotron facilities to achieve high spatial resolution. Spatial resolution of an image is not only achieved by having high pixel resolution, but also by having high contrast and a high signal-to-noise ratio, so as to be able to distinguish between two neighboring features, in space, with high fidelity. In XRM, the physical and crystallographic properties of state-of-the-art scintillators are tuned for objectives of varying magnifications, allowing the useful part of the target energy spectrum to be converted into visible light with higher quantum efficiencies than in conventional flat panel detectors. These photons are then further magnified in the objectives, which are subsequently registered with a CCD.

It is precisely this feature—optical magnification with enhanced spectral properties—which allows XRM to achieve high spatial resolution and high contrast even at large working distances (see Figure 3).

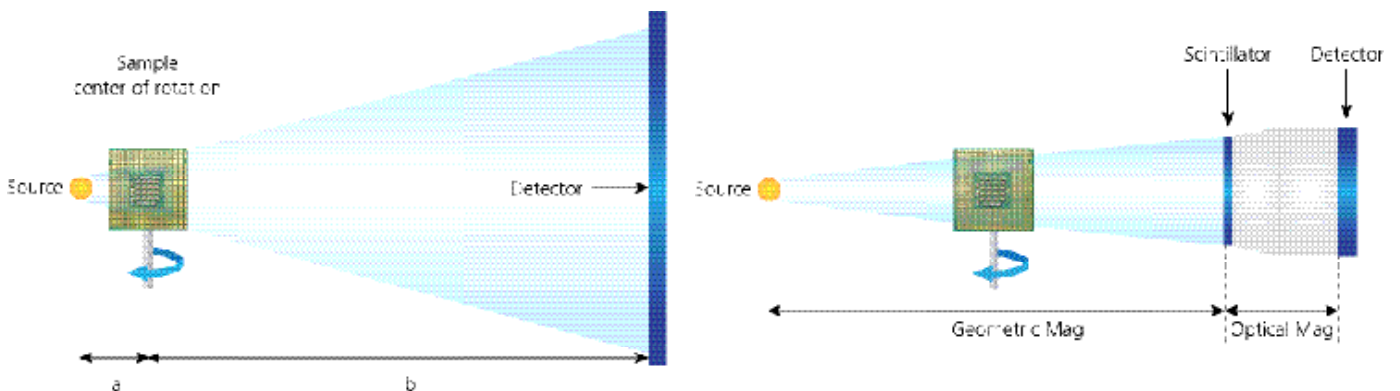


Figure 3 XRM does not depend on geometric magnification to achieve high spatial resolution.

Effects of imaging parameters to image quality and scan times

All CT reconstructed scans are subject to various imaging artifacts that can affect overall image quality. Generally speaking, 3DIC packages require better image quality (higher spatial resolution and higher contrast) than its 2DIC counterparts, so understanding artifacts and their reduction techniques is essential to achieve SEM-like images non-destructively. Although not discussed here, among the most common types of CT artifacts affecting semiconductor samples are beam hardening, under sampling, and photon starvation [4]. Likewise, understanding the effects that imaging parameters have on the reconstructed data can help understand the capabilities and limitations of XRM as it applies to replacing physical cross-sections in specific applications in 3DIC packages and as the technology evolves to address gaps in in-line metrology.

a) Energy (kV): The energy of the source determines the extent to which the X-rays penetrate through the sample, which in turn determines the percent absorption and percent transmission through the sample. If a sample is highly attenuating—composed of high-atomic number (Z) materials or if it is thick—then higher energy X-rays are needed to penetrate the sample and obtain acceptable values of

transmission. During reconstruction, a grey scale value is assigned to each voxel based on the percent transmission of X-rays passing through each voxel at each angle of projection in the tomography. These grey scale values determine the relative contrast that distinct features and/or materials will display in the virtual cross-section image. An ideal tomography has transmission values between 25% and 35% through all the angle projections through the feature of interest. For example, low energy is required to generate absorption contrast between air bubbles and low-attenuating underfill layers. If high energies are used instead, the transmission through the underfill layer would be too high (<90%), creating very little contrast in the air bubbles. Alternatively, high energy is needed to generate contrast between voids and solder in solder bumps (see Figure 4). If low energies are used, the transmission will be too low and little signal will go through the sample. Filters that absorb the lower energies from the X-ray spectrum are commonly used to boost the transmission through high-attenuating materials by making the average energy of the X-ray beam higher. Filters are also used in the same way to reduce beam hardening artifacts [4].

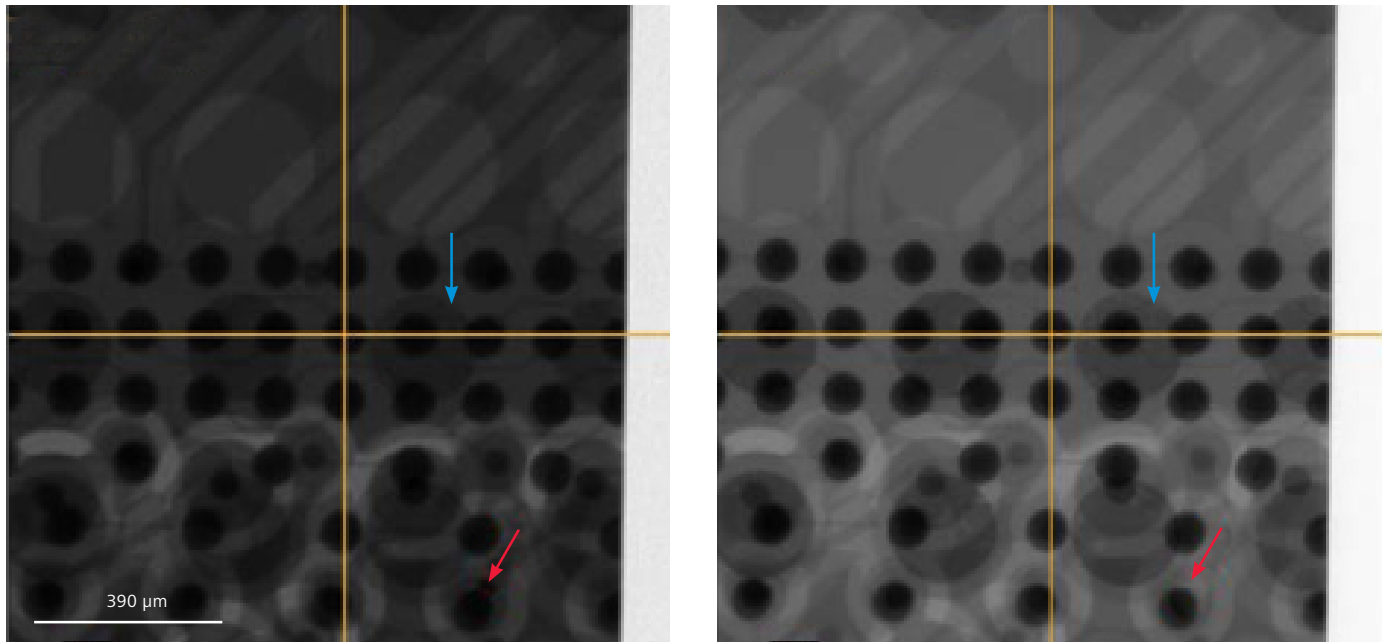


Figure 4 The left image shows the transmission of a TSMC test vehicle sample using a source setting of 40 kV. The right image shows the same FOV at 150 kV (all other image acquisition parameters remain constant). The image on the right shows better contrast between the Cu pads and solder bump as highlighted by the red arrows. The blue arrows show how voids become more distinctly visible (better contrast) at higher voltages.

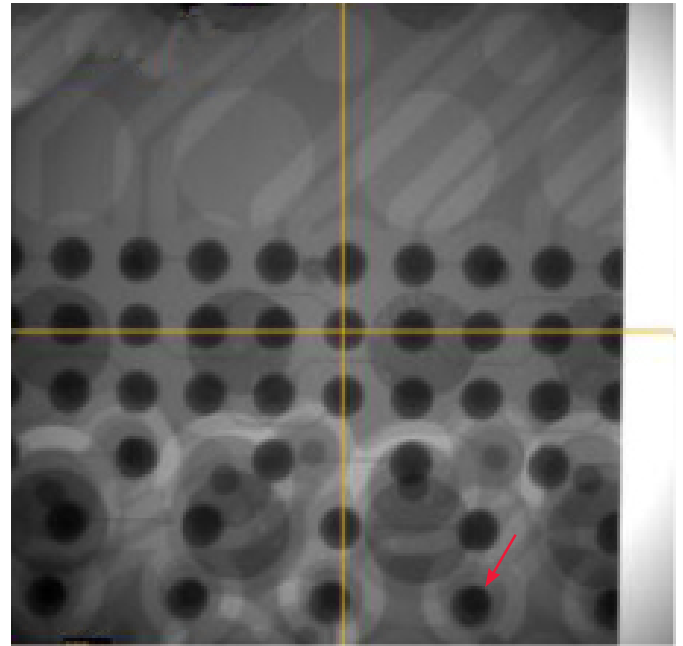
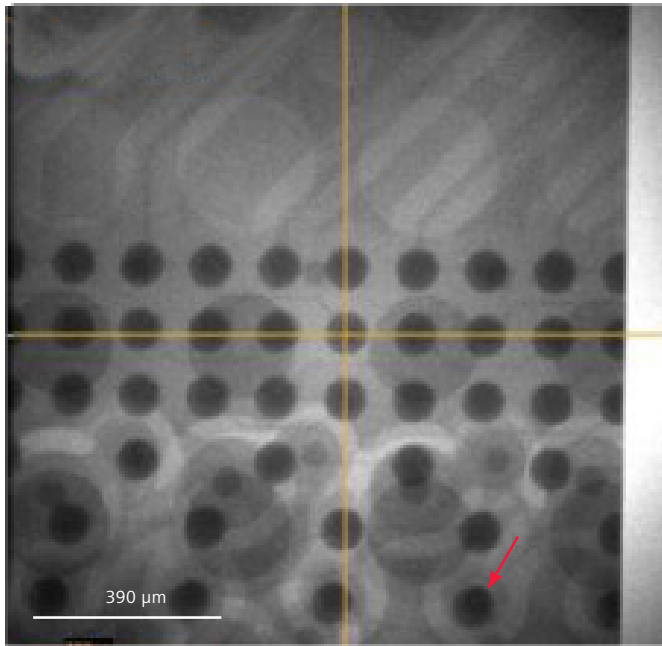


Figure 5 Effect of photon starvation. Despite having the same transmission (and relative contrast) value, the image on the right is much higher quality. While the left image shows a 2D projection collected using an exposure time of 0.01 seconds, the image on the right was collected using an exposure time of 5 seconds. A high signal-to-noise ratio is required to distinguish a small feature against its background noise. This is particularly important to distinguish submicron measurements of voids or cracks in 10 μm through-silicon vias, for example.

b) Signal-to-noise Ratio: After the X-rays are converted into photons by the scintillator, they are condensed by the objectives and registered in the CCD. The number of photons that hit each pixel of the scintillator is referred to as counts.

A good quality image has between 3,000-10,000 counts to make sure that each pixel is clearly registered as feature or background and not noise. Having less-than-ideal counts leads to spatial artifacts commonly referred to as photon starvation depicted in Figure 5. Counts are linearly proportional to time of exposure. For example, 10x the exposure time for a projection will lead to 10x the number of counts (and a clear improvement in the signal-to-noise ratio). Counts are also affected by the distance between the source and detector—longer exposure times are required to get the appropriate counts in larger samples. For this reason, it is always best to minimize the distance between the source and detectors while maintaining the desired geometric magnification ratio. Counts also behave proportionally with the power setting of the source—the higher the power, the higher the counts. Finally, using X-ray source filters (which is highly recommended to improve transmission and reduce artifacts)^[4] inevitably reduces the total photon counts. Therefore, a tradeoff exists between using thicker filters to boost transmission of highly attenuating samples and using no filters to improve the signal-to-noise ratio.

c) Geometric and Optical Magnification: The same total magnification of 40X can be achieved by using a 4X objective lens with geometric magnification of 10X or by using a 10X objective lens with geometric magnification of 4X, for example, as demonstrated in Figure 6. The final selection of which objective to use will be determined by the sample size and the desired spatial resolution.

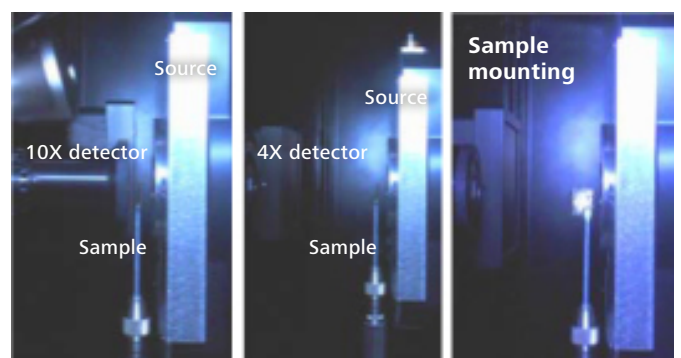


Figure 6 The system configuration of the left uses less geometric magnification and a higher objective to achieve an unspecified spatial resolution. The system configuration of the middle uses more geometric magnification and a lower objective to achieve the same spatial resolution as the system on the left. The image on the right shows a TSMC test vehicle package as it was mounted on the equipment at 90°.

d) Field of View and Voxel Size: FOV and voxel size are inversely proportional, much like in all other microscope systems—highest resolutions are limited to small FOVs, while large FOVs can only yield low resolutions. State-of-the-art graphics cards are used to handle the memory-intensive computations needed for reconstructing a large number of 2D X-ray projections. Reconstructing large FOVs with small pixel sizes would take too long (upwards of 1 hour), the generated files would be too large (upwards of 100 GB) and provide an excessive amount of data that would not be used. Generally speaking, the resolution of a scan is chosen first—based on a priori knowledge of the size of the suspected defect—dictating the size of the FOV. It is because of this limitation—achieving large FOVs in practical times—that existing XRM equipment architectures are best suited for FA labs, and not for in-line metrology of large samples (i.e. 300 mm wafers). It is worth mentioning that XRM is capable of achieving high spatial resolutions in intact wafers, but the times needed to collect good quality CT data are not very practical. Generally speaking, in current XRM equipment architectures it would take 3-20 hours to image a submicron feature in an intact wafer, and it would all depend on location of the ROI in the wafer (which will vary the axis of rotation and hence the geometric magnification) and the materials used in the wafer (which will dictate the energy and exposure time needed). The route to achieving fast, high-resolution 3D X-ray metrology is to improve the TPT of single measurements (i.e. one CT scan) with small ROIs by making software and hardware improvements and by innovating new equipment architectures.

Experimental

An 18 x 21 mm TSMC test vehicle sample with suspected failure locations was imaged using Xradia 500 Versa microscope. A 210 minute scan was setup using 0.7 $\mu\text{m}/\text{voxel}$ spatial resolution, $\sim 30\%$ transmission and $\sim 5,000$ photon counts through the 0° view using a total of 1600 projections from -90° to $+90^\circ$. The raw data was then reconstructed into a 3D dataset in less than 3 minutes. The resulting 3D model is shown in Figure 7.

Upon reviewing the 3D data set, several defects were clearly visible in the scanned region, including a solder bump non-wet and heavy voiding in the BGA layer. A virtual cross-section image was exported and used to compare to the same location after physical cross-section took place as shown in Figures 8-9.

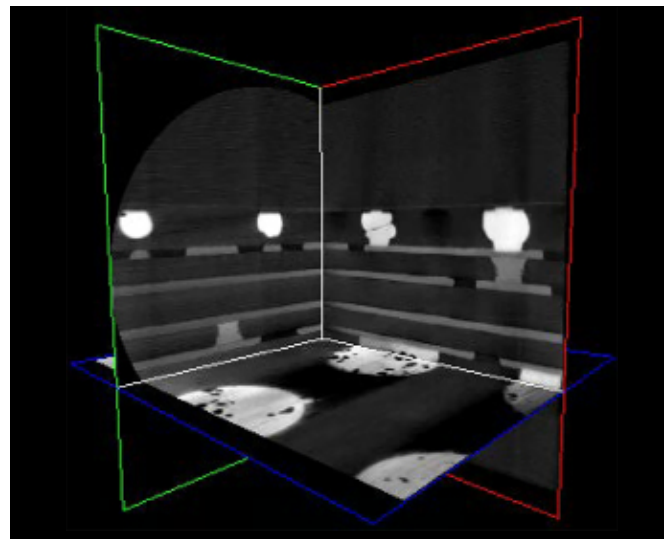


Figure 7 Virtual 3D model of the internal structure of TSMC test vehicle sample. The FOV is 0.7 mm^3 and the spatial resolution is $0.7 \mu\text{m}/\text{voxel}$. The three colored boxes represent orthogonal, virtual cross-section planes through the volume. The 3DViewer Software makes it easy to navigate through the volumetric data to find the non-wet defect as well as large voids in the BGA bumps.

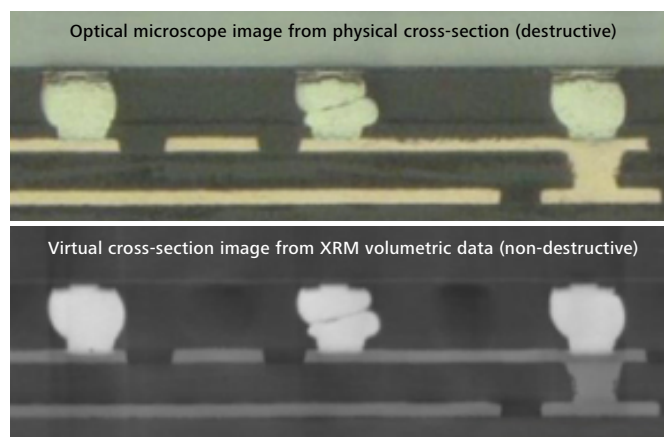


Figure 8 Comparison between images collected with an optical microscope taken after destructive cross-sectioning (top) and a virtual cross-section image taken from the non-destructive XRM computer tomography scan (bottom). The red arrow points to a $\sim 2 \mu\text{m}$ void between the Cu pad and the solder bump that was missed by physical cross-section. High-resolution volumetric data is powerful because it allows the user to review an infinite number of virtual cross-sections through any direction through the volumetric dataset, shortening the time that it takes to isolate a defect and determine the cause of package failure, all in one scan.

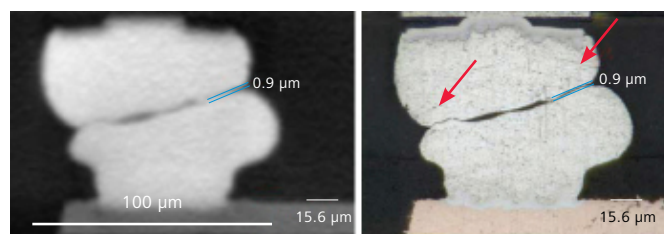


Figure 9 The left image is a zoomed-in image of Figure 8 while the right image shows an optical micrograph image of the defect taken with a higher objective lens. Note the high contrast and spatial resolution attained with XRM, where a $0.9 \mu\text{m}$ non-wet separation can be clearly measured. The red arrows show polishing defects caused from physical cross-section. These artificially introduced defects can often times make it difficult to determine the location and size of the actual defects. Since XRM is non-destructive, the sample is intact and impervious to the introduction of polishing defects.

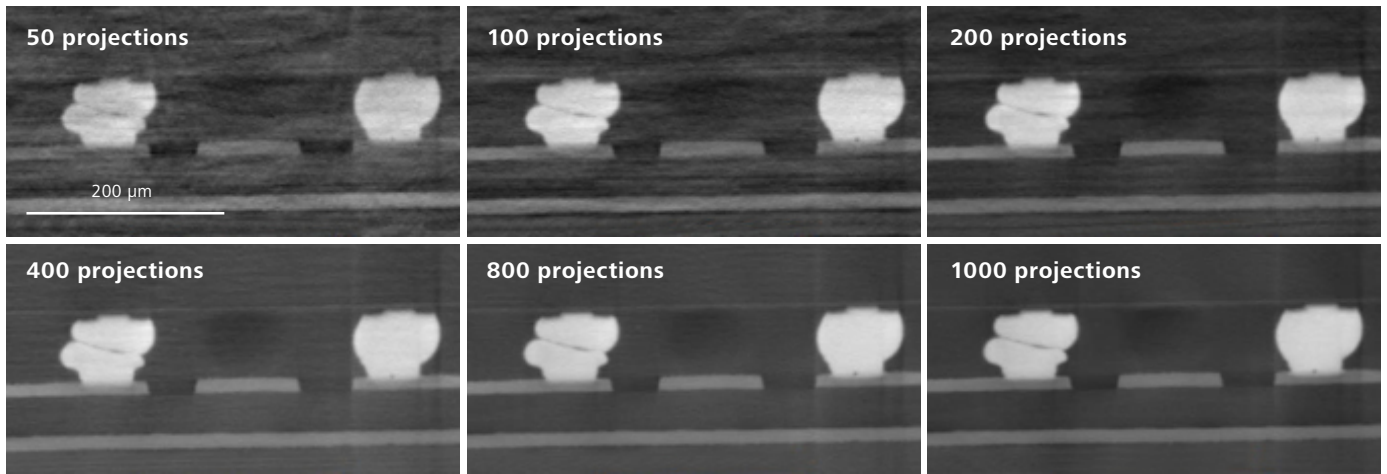


Figure 10 Data reconstructed from the original scan using 1600 projections showing the results that were obtained from running a 210 minute scan; 800 projections simulating a 110 minute scan; 400 projections simulating a 55 minute scan; 200 projections simulating a 30 minute scan; 100 projections simulating a 15 minute scan; and 50 projections simulating an 8 minute scan. The set of images clearly depicts the introduction of under sampling CT artifacts. Small number of projections and/or limited angle scans (as in the case of laminography equipment architectures) will introduce these under-sampling artifacts during data reconstruction. These artifacts become more critical if the features being measured are below 10 µm.

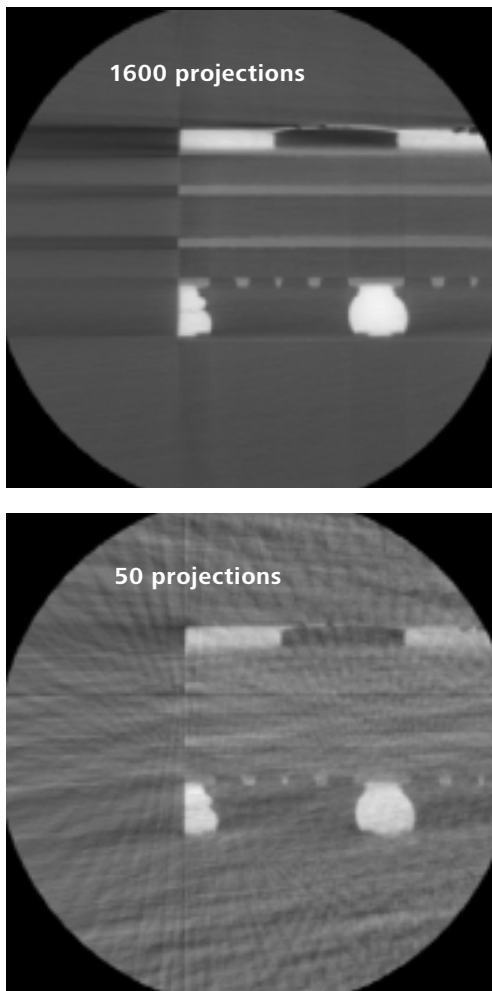


Figure 11 Different virtual cross-section of entire FOV of the scan where under-sampling artifacts are more noticeable.

The thickness of the virtual cross-section image plane is 0.7 µm. Using the same data collected in the experiment, it is possible to simulate shorter scan times—by removing projections (see Figure 10). Despite compromising image quality by introducing under-sampling defects for improved TPT, the non-wet defect can still clearly be seen and measured. Figure 11 shows a different virtual cross-section of the entire FOV of the scan.

Conclusions

Detector technology advancements in the past five years have allowed X-ray microscopes to bridge the inspection gap between high-resolution, destructive SEM and low-resolution, non-destructive MicroCT capabilities. XRM is routinely being used to replace physical cross-section of complex multi-layered devices with fine pitch interconnects in 3DIC packages. Understanding the effect that imaging parameters have in the resulting image quality of a scan for a specific sample type can lead to the reduction of data collection and reconstruction times, thus improving overall UPH, providing unprecedented capabilities to FA labs and package development facilities. Furthermore, optical magnification with enhanced spectral properties offered by state-of-the-art detectors is enabling high resolution imaging at large working distances, enabling the imaging of intact wafers with high resolution; though TPTs are still impractical for this application, the capability now exists. As XRM technology becomes pervasive in FA labs, more studies correlating XRM with SEM and optical images will validate the performance of XRM and the industry will continue to use this non-destructive technique as a workhorse to replace physical cross-section. Finally, improvements in software, hardware and equipment architectures will continue to evolve to make XRM technology more compatible with high-volume manufacturing metrology needs.

References

- [1] K. Fahey, R. Estrada, L. Mirkarimi, R. Katkar, D. Buckminster, M. Huynh, "Applications of 3D X-ray microscopy for advanced package development," IMAPS 2011 44th International Symposium on Microelectronics, October 9-13, 2011.
- [2] A. Merkle, J. Gelb, "The ascent of 3D X-ray microscopy in the laboratory," *Microscopy Today* 21(2) 2013, pp. 10–15.
- [3] M. Cason, R. Estrada, "Application of X-ray microCT for non-destructive failure analysis and package construction characterization," IEEE Physical and Failure Analysis of Integrate Circuits (IPFA) 2011, pp. 1–6.
- [4] F. Boas, D. Fleischmann, "CT artifacts: causes and reduction techniques," *Imaging Med* 4(2) 2012, pp. 229–240.

Non-destructive 3D X-ray Imaging for Advanced Packaging Failure Analysis

Cheryl Hartfield
Carl Zeiss Microscopy

Daniel Nuez
Xilinx, Inc.

Introduction

Packaging of integrated circuits is growing more and more complex – and housing multiple die in a single package is just one challenge chipmakers face. Typically, these die are connected in complex ways, and chipmakers must contend with shrinking feature sizes and interconnects, escalating device density and package size, thinner layers, and a widening variety of materials.

As a result, failure analysis (FA) on advanced packages is becoming increasingly difficult. The goal of FA is to isolate where the failure is located, and then figure out what it is and why it happened – its root cause. Visualization of defects aids determination of the root cause. Packages are essentially opaque boxes containing electrical connections. Often, to visualize a defect in the electrical path, physical failure analysis (PFA) is applied.

Maintaining integrity of the defect site is critical. If a sample is cut or reduced in size, further electrical analysis may not be possible, and the structure may be disrupted by introducing artifacts or changing the stress profile from that of an intact sample. Conventional non-destructive methods have become less effective at visualizing defects in many of today’s packages, creating a significant need for new non-destructive approaches such as 3D X-ray microscopy (XRM).

Benefits of X-ray microscopy

In the typical board- and package-level FA lab workflow, failures are evaluated non-destructively prior to destructive analysis (Figure 1). The most common non-destructive PFA techniques for isolating and visualizing defects are optical inspection, 2D X-ray, and scanning acoustic microscopy (SAM). Due to increased package complexity, these imaging techniques are becoming less effective.

XRM, a relatively new FA technique, uniquely provides a high-resolution, non-destructive method to find and image defects in 3D. It thereby provides critical knowledge to guide next steps. Application of XRM typically fits between fault isolation and root cause determination (Figure 1).

Once the fault location is isolated, traditionally, a next step is a visit to the “coroner’s office” – that is, PFA techniques that destroy the sample are used to investigate the root cause of the failure. The techniques cited on the far right side in Figure 1 all involve physically cutting, drilling or otherwise altering the sample in some way. If the fault is not properly located, there is no second chance to find it unless another package is sacrificed.

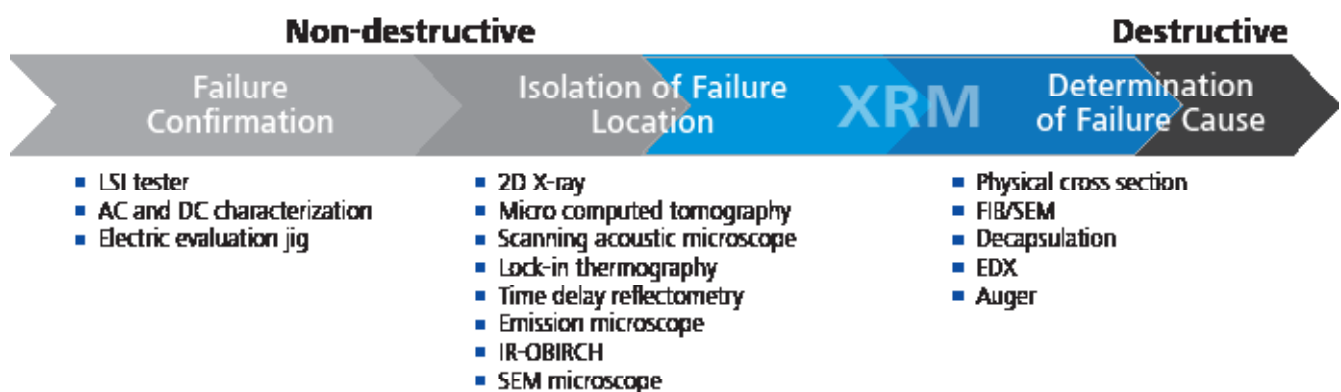


Figure 1 Acceptance of 3D X-ray microscopy is growing for failure analysis.

Providing 3D intelligence ahead of destructive analysis is a key benefit of XRM. It enables higher success rates in cross-sectioning and finding root causes. Visualization of defects by 3D XRM can even eliminate the need to perform PFA, saving time and resources. The case study included in this article illustrates the effectiveness of 3D XRM in the FA workflow.

Visualizing defects non-destructively with virtual cross-sections

The power of 3D tomography comes from its ability to provide virtual cross sections, revealing the details inside structures. Figure 2 provides a simplified overview of the XRM tomography process. Figure 2a shows that data is acquired by collecting 2D projection images from a rotating sample positioned between an X-ray source and a detector (the yellow dot in Figure 2a). The XRM detector is composed of scintillator-coupled optical microscope objectives combined with a charge-coupled device (CCD) camera. The X-rays pass through the sample and hit the scintillator mounted on the objective lens. The scintillator converts the pattern resulting from X-rays transmitted through the sample into the optical image captured on the right (Figure 2b). The sample is then rotated slightly, the image captured again, and this process is repeated through up to 360 degrees of rotation. The resulting group of projections – typically, between 1,000 and 2,000 – are then processed by algorithms to mathematically reconstruct the 3D volume (Figure 2c).

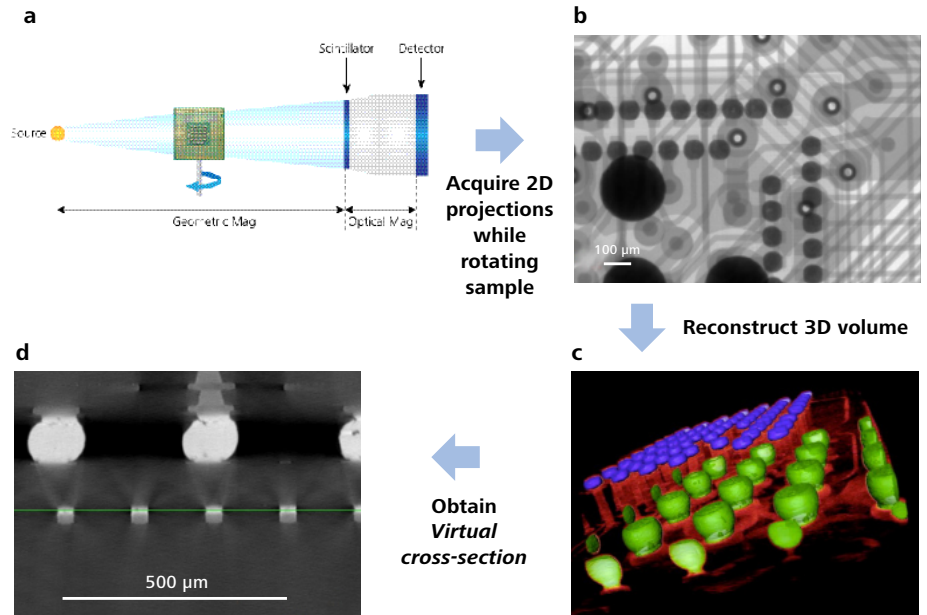
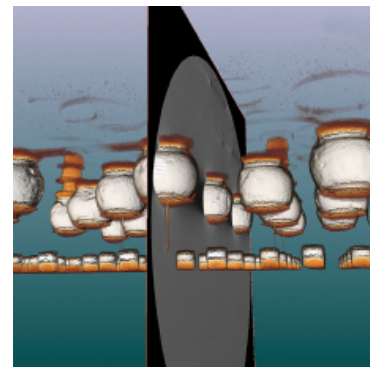


Figure 2 XRM 3D tomography yields highly informative visual information about failures, non-destructively.

Reconstructed 3D dataset



Virtual cross-section

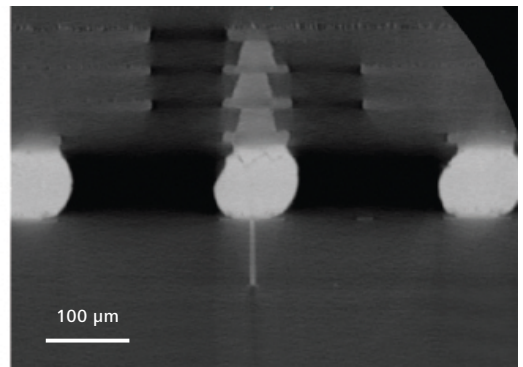


Figure 3 Using XRM, any plane through the 3D data may be viewed as a virtual cross section.

The time required for the entire process is variable – typically ranging between 30 minutes and 8 hours – depending on the number of projections and how much time is spent per projection. From the resulting 3D volume, one can view any number of horizontal or vertical cross sections through the sample (Figure 2d) – essentially, isolating any desired sliver of the 3D volume. Therefore, details of fault locations can be visualized without destroying the sample.

As an example, Figure 2d shows a virtual cross-section of a 2.5D interposer stack. The virtual cross-section plane can be moved interactively through the 3D dataset in any of the three orthogonal directions (x, y, z). This allows localization of defects to specific areas, such as the substrate-side or chip-side of a flip-chip bump, and aids understanding of the failure mechanism. Figure 3 provides another look at how a virtual cross section is obtained from the reconstructed 3D dataset.

XRM vs. microCT

Micro-computed tomography, or microCT, is another approach to obtaining 3D images. However, as Figure 4 illustrates, XRM offers significant resolution advantages compared to microCT. To achieve high resolution in microCT systems, high-geometric magnification is required. This involves placing the sample very close to the source (Figure 4b) and moving the detector as far away as possible – this ratio determines the magnification and, thus, the resolution of the image. With microCT, large samples are challenging to image at high resolution. As samples become larger, they must be moved further away from the source so they can be rotated without colliding with it. As the sample is moved away, there is a linear reduction in the magnification, which, in turn, lowers the resolution (Figure 4b).

The advantage of XRM is that high-resolution images can be obtained from fully intact large samples that are positioned further away from the source (Figure 4a). The scintillator-coupled

microscope objectives provide the magnification necessary to retain resolution versus depending upon geometric magnification alone. With XRM, resolution remains relatively independent of the package size, and high resolution can be maintained with large sample sizes. This capability represents the core value of XRM vs. microCT technology.

Increasing the success rates of PFA

The following case study demonstrates the benefits that 3D XRM offers to chipmakers. In this instance, a 2.5D interposer test chip with microbumps was used for packaging development and process optimization. In the center of Figure 5 is the package computer-aided design (CAD) layout, showing microbumps and larger C4 bumps. A short has been isolated to the spot depicted in the green box at left. At right is the 2D X-ray image – the three microbumps are visible inside the C4 bump, in the same orientation, but it is impossible to see where the short is actually located.

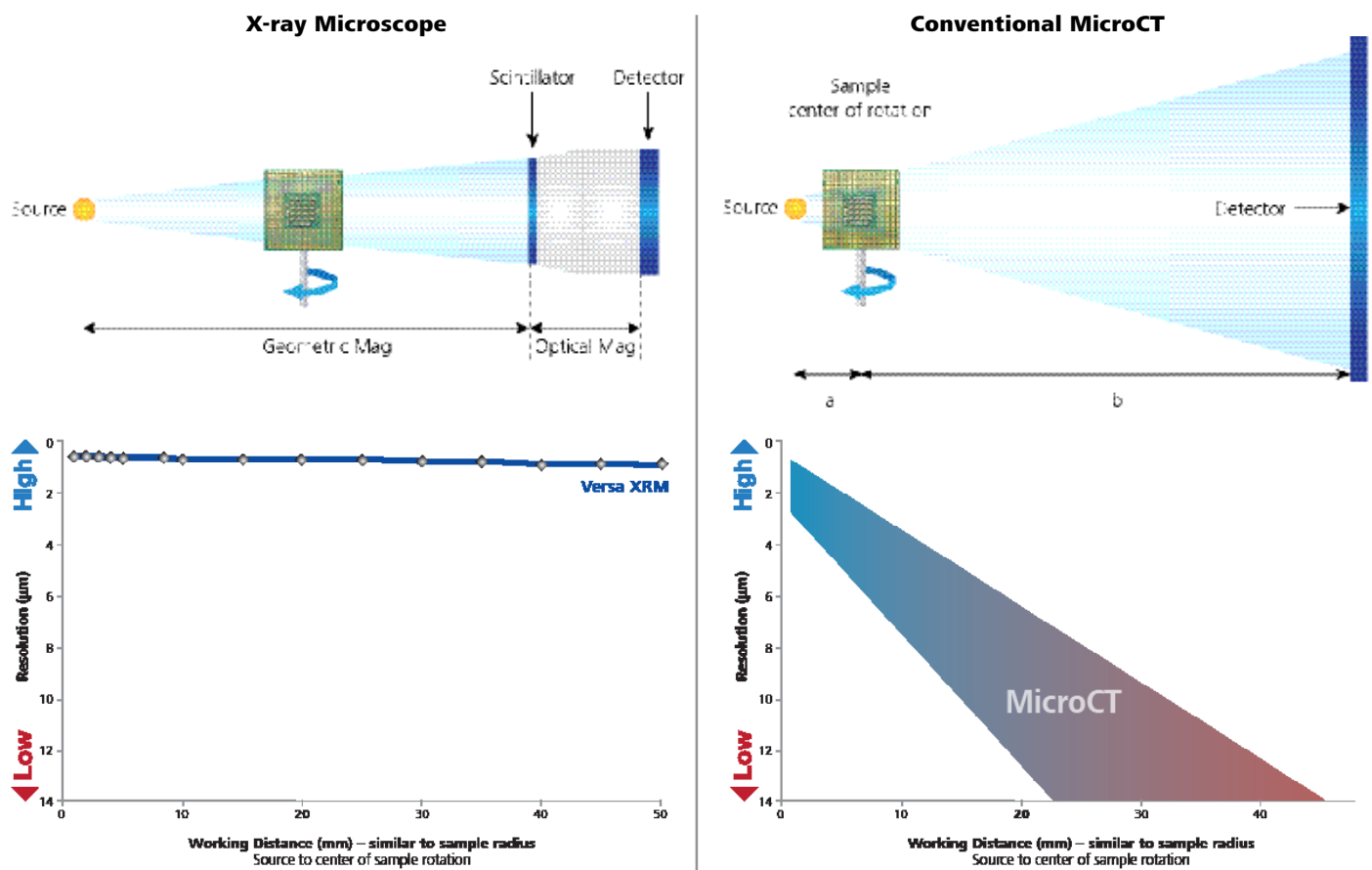


Figure 4 XRM does not depend on geometric magnification to achieve high spatial resolution.

The red dotted line in the middle image indicates the direction of the physical cut performed with PFA in an effort to visualize the short. As the orange line labeled “solder extrusion” shows – and as was later determined using XRM – the short from one microbump to another exists at an angle. XRM also revealed that the size and mass of the short was below the detection limits of the 2D X-ray system.

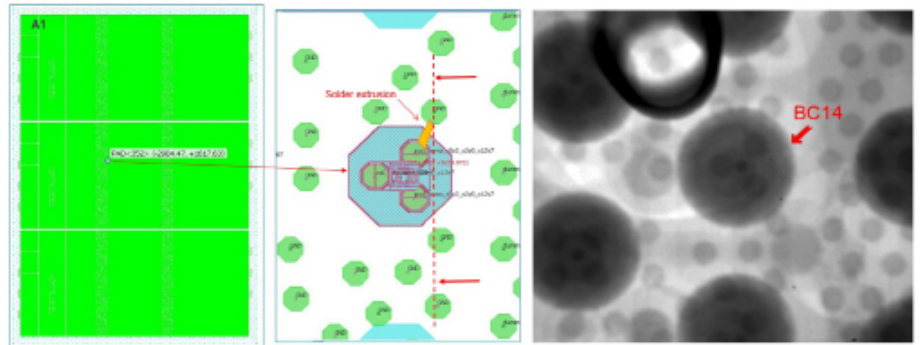


Figure 5 In a sample 2.5D interposer chip, an electrical failure was found at pin BC14, but 2D X-ray inspection failed to show any structural anomaly.

The failure analyst repeatedly cut and polished the sample to get as close as possible to the failure site. An anomaly in the form of solder extrusion was observed (see Figure 6) and suspected to be the cause of the short. An optical image is on the left, and a SEM image is on the right. Visual evidence of a short across adjacent bumps is missing in both optical and SEM images. The analyst continued to polish about 10 microns further, and as Figure 7 shows, polished through evidence of the short. Although the electrical data pointed to the short’s general location, more precise information was needed to successfully confirm the short by destructive PFA.

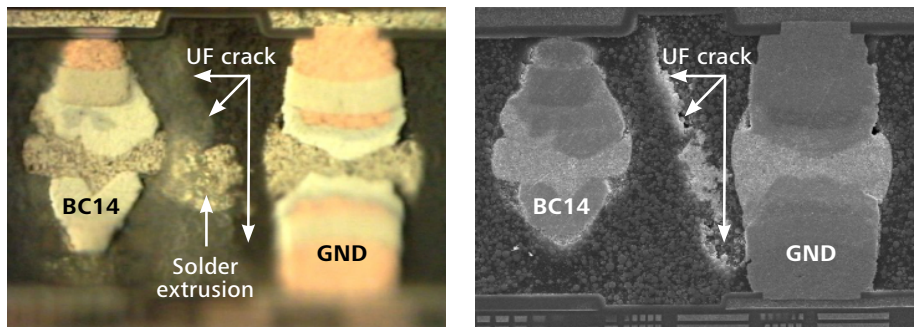


Figure 6 The first cut using PFA revealed the solder extrusion, but not the bump-to-bump connection, requiring further cutting and polishing.

3D XRM can reveal details of a solder bridge (location, size and orientation) prior to destructive analysis. This information can then guide and enable successful execution of a precise cut into the solder bridge. As Figure 7 shows (right image), there was evidence of solder extrusions in adjacent bumps. Before attacking the sample further with continued polishing, a defective area was imaged by 3D XRM using submicron voxels.

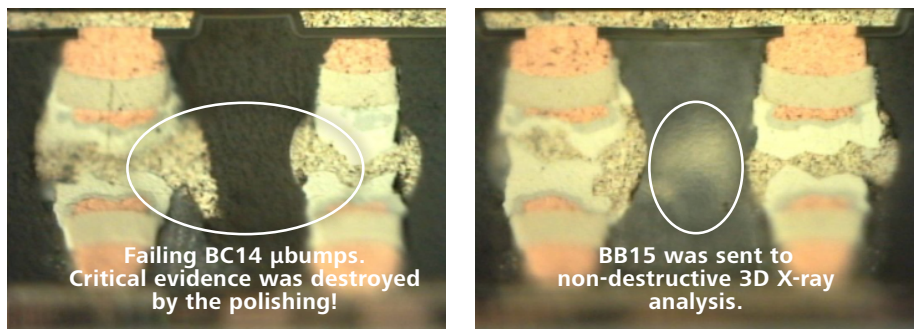
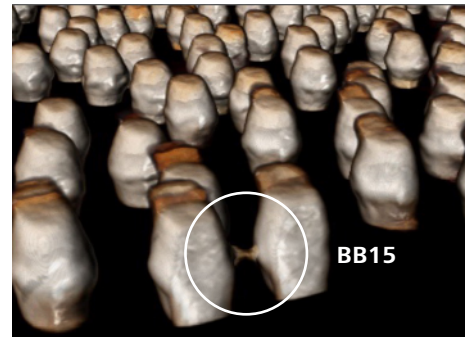
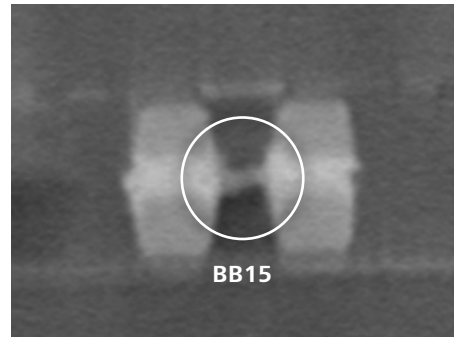


Figure 7 The second polish destroyed the physical evidence of a microbump short on pin BC14. Non-destructive 3D XRM tomographic imaging was performed on adjacent bump BB15 due to evidence of solder extrusion in the cross section’s optical image.

The 3D rendering in Figure 8 shows the exact location and orientation of the short, which guided the subsequent destructive cross-sectioning angle and resulted in a successful FA report.

High resolution 3D XRM was used to confirm the solder bridge defect at BB15



Failed Pin	BC14	BB15
3D X-ray integrated FA		XRM clearly visualized the solder bridge defects without cutting or downsizing the sample
Conventional FA	First cut revealed solder extrusion, but evidence of solder bridging was not obtained in further polishing due either to removal of evidence or to analysis in the wrong plane	Further cross-section is possible, guided by 3D XRM data

Figure 8 3D XRM data confirmed the defect with no destruction of the chip sample.

Summary

Package technology is growing in complexity and the FA workflow needs to adapt to the new requirements. Conventional FA involves cutting into samples and polishing the edge to the approximate location of the failure. Then SEM and/or optical micrographs are used to capture high-resolution 2D images in order to help determine the failure’s root cause. While valuable for some applications, this approach is destructive – it provides a single chance to choose the right cutting orientation that will expose the failure for imaging. Moreover, the process may introduce artifacts from cutting and polishing that can hinder root cause determination. Defects may be missed, leading the failure

analyst to conclude that no defect could be found. With its high-resolution and non-destructive properties, 3D XRM imaging and analysis has become increasingly commonplace in FA workflows, particularly for advanced 2.5D and 3D packaging architectures. By providing detailed 3D images of failure locations, it is a valuable precursor to – and in some cases, can completely replace – physical cross-sectioning.

A Breakthrough in Resolution and Scan Speed: Overcome the Challenges of 3D X-ray Imaging Workflows for Electronics Package Failure Analysis

Allen Gu, Gerhard Krampert, Susan Candell, Masako Terada,
Carl Zeiss Research Microscopy Solutions, 5300 Central Parkway, Dublin, CA 94568, USA

Thomas Rodgers
Carl Zeiss Microscopy GmbH, Rudolf Eber Str. 2, BG 41/1, 73447 Oberkochen, Germany

Abstract

Non-destructive 3D X-ray microscopy (XRM) has played an important role in advances of semiconductor packaging development and failure analysis [1-3]. Over the past decade, the IC industry has increasingly focused on packaging innovations to improve device performance and cost-effectiveness. The emergence of novel 2.5D, 3D and recent heterogeneous integration packages challenges the existing X-ray imaging and characterization workflows because I/O interconnects such as small-volume solders and hybrid Cu-to-Cu bonds are more miniaturized in densely packed packages. In this report, we will introduce a new scintillator material coupled with a 40X objective lens (referred as 40X-P), integrated in an XRM detector system, capable of delivering better spatial resolution and contrast than the traditional Cesium Iodide (referred as CsI) scintillator based X-ray detector. Several commercial semiconductor packages will be imaged and analyzed with both the new 40X-P and a standard 40X objectives for comparison. We will also demonstrate that the data acquisition with 40X-P can be accelerated by a factor of four with a deep learning reconstruction method, improving its efficiency in failure analysis applications.

Introduction

Semiconductor packaging technologies have been the driving force to propel advances of electronics device performance, while traditional silicon downscaling has been slowing down. The IC packaging industry faces a paradigm shift in design, manufacturing, and inspection techniques to adopt more than Moore packaging innovations. Among many newly emerged interconnection techniques, fine pitch interconnection, 3D stacking, and solderless hybrid bonding are particularly attractive for the advantage to increase I/O density with the bridged size gap between Si and package. However, the IC industry faces the challenge to find an effective non-destructive solution for imaging these relentlessly miniaturized interconnects and defects.

3D XRM has become the preferred solution for semiconductor package failure analysis because of its non-destructive and high resolution capabilities. Unlike conventional computed tomography techniques, where spatial resolution solely relies on geometric magnification, XRM utilizes a unique two-stage magnification mechanism to achieve high resolution over large working distances. With both geometric and optical magnification, XRM enables submicron resolution across the normal range of semiconductor package sizes. XRM system resolution and contrast are defined by a variety of contributing factors such as source, detector, scan conditions, etc. In this paper, we focus on both the resolution and contrast improvement enabled by a new scintillator material coupled with a 40X objective lens. It is capable of delivering significantly better spatial resolution and contrast over a broader range of X-ray energies than the traditional CsI scintillator based detector. This is achieved via the higher density (i.e., higher average z-number) of the new scintillator material compared to CsI. Because of the heavy atom compositions, it converts high-energy X-ray photons to visible light better than the traditional CsI, making it better resolution and contrast even at high energies.

The first test vehicle was a commercially purchased 9x14x1.1 mm DRAM memory package with four layers of microbump and TSV stacks. The second test vehicle is a commercial 22x26x1 mm embedded multi-die interconnect bridge (EMIB) package with a heterogeneously integrated high-bandwidth memory and a graphics processor. We will demonstrate that the new 40X-P delivers better 2D and 3D resolutions and contrast of X-ray microscopic images on these test vehicles. In the previous studies, we reported the deep learning based reconstruction method can be used to speed up the scan throughput by a factor of four [4-6]. Here, we apply the reconstruction workflow to reduce the scan time of the 3D data acquired with the 40X-P objective.

Instrumentation and Setups

In a typical data acquisition with XRM, a sample rotates by 180 (\pm fan angle) or 360 degrees, and a set of projection images are acquired by an X-ray detector system. A scintillator screen coupled with an optical objective is utilized to convert X-ray photons to visible light, and the magnified projection images are captured by a CCD camera. These 2D images are mathematically reconstructed to 3D data. For the comparative studies, both 40X-P and standard 40X objective lenses were installed on a same turret for all imaging work. The standard procedures of beam alignment and objective calibration were followed.

Figure 1 shows the example 2D projections on a standard resolution target obtained with a standard 40X (Figure 1a) and the 40X-P (Figure 1b) objectives at 120 kV and a LE6 X-ray filter. Because of the superior performance at high energies of the new 40X-P, 500 nm spatial resolution was achieved. The measured modular transfer function of 40X-P only drops off at highest levels of resolution, indicating that the new objective maintains superior contrast in the high spatial frequency range. Although the peak performances of both objectives are achieved at a low energy, high energy performance is more critical in imaging high-density IC packages.

Results and Discussions

Because each projection contributes to the image quality of a reconstructed volume, it is important to optimize 2D X-ray projection views prior to 3D data acquisition. Figure 2 shows the two projection images on a commercially purchased DRAM package, which was not trimmed or prepared in the imaging work. Both images were acquired at 70 kV with a LE2 source filter at 0.49 $\mu\text{m}/\text{pixel}$ resolution for a comparison.

The image acquired by the 40X-P objective in Fig. 2b looked much crispier than the image with a standard 40X objective in Figure 2a, especially on the edges of Cu pillars and microbumps. DRAM packaging architectures have utilized a small-volume soldering technique to stack multiple layers of dies through a thermocompression bonding process. The bond linethickness of $\sim 15 \mu\text{m}$ and TSV with a diameter of 5 μm have been seen in advanced DRAM packages.

However, imaging small interconnects and internal defects of these packages has been challenging because of resolution limitations in microCT and XRM systems. Prior to the 40X objective tests, we used low-magnification objectives of 0.4X and 4X to precisely localize the scan region (Figure 3a) for the data acquisition with 40X objectives. With the X-ray imaging parameters in Figure 2, the sample was scanned with both 40X objectives.

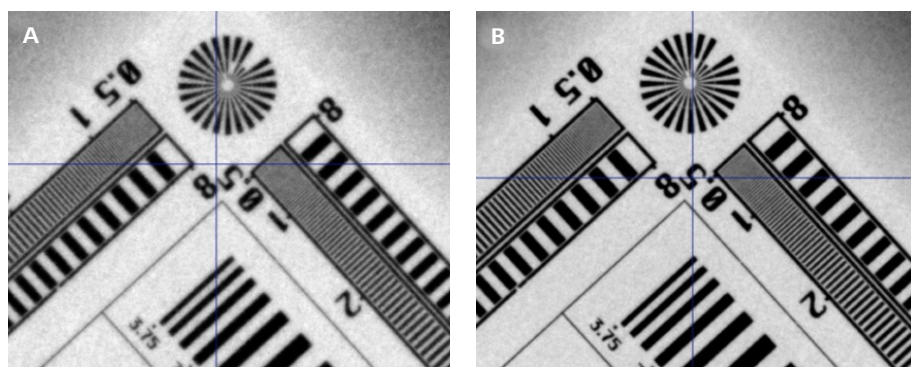


Figure 1 Resolution and contrast performance comparison. A) A 2D projection view with a standard 40X objective lens at 120 kV X-ray energy and a LE6 filter. B) 2D projection view with the 40X-P at the same energy and filter. The test sample was a ZEISS standard resolution target.

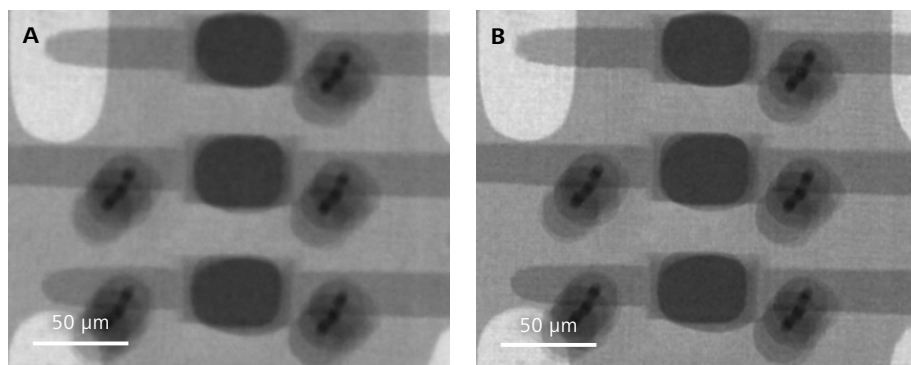


Figure 2 Resolution performance comparison of 2D projections on the DRAM package sample. A) with a standard 40X objective lens at 70 kV and a LE2 filter. B) with the 40X-P at the same energy and filter.

Figure 3c is a virtual cross-section image of TSVs and microbumps acquired with the 40X-P objective, clearly showing the resolution and contrast improvement over the image with a standard 40X objective (Figure 3b). Furthermore, the voids in microbump solders appeared much better defined than the image of the voids acquired by the standard 40X. The material phase separation can be clearly seen on the planar view acquired by 40X-P objective in Figure 3e, while the same virtual slice shows a blurry image on the phase separation in Figure 3d.

We reported a lab-based nanoscale tomographic technique to explore the applications of imaging semiconductor packages and back-end-of-line (BEOL) structures [7-8]. About 100 nm features can be effectively visualized, but the technique requires a significant sample preparation. Because the non-destructivity is highly valued in failure analysis applications, we studied the 40X-P performance to image BEOL structures of an EMIB package, which are not among typical regions of interest with XRM. Figure 4b shows more promising resolution and contrast performance with the 40X-P objective, compared with the image performance by a standard 40X (Figure 4a). The metal lines and small submicron features are clearly resolved with greater certainty with the 40X-P objective than a standard 40X.

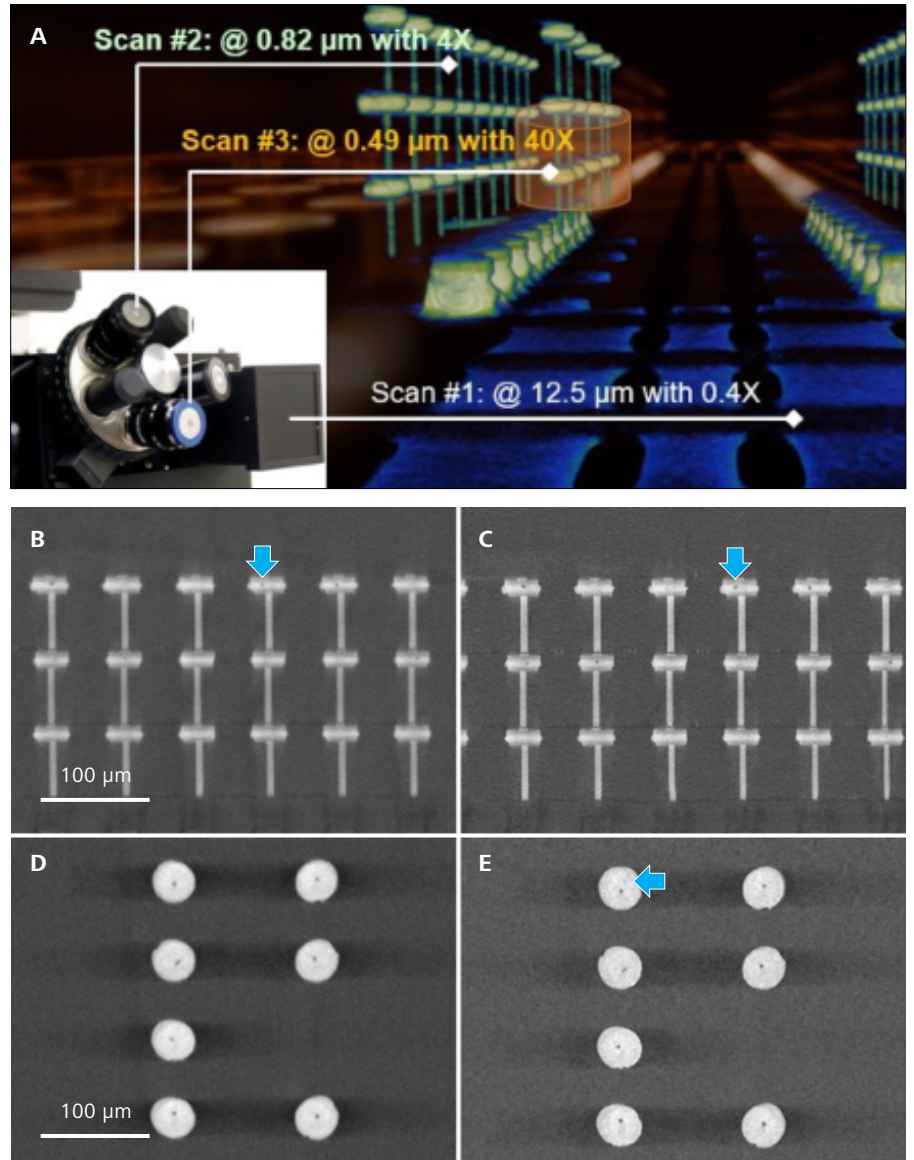


Figure 3 A comparative study of the 40X-P objective to a standard 40X objective on the DRAM package sample. Two 3D tomographies with 40X objective were acquired at 0.49 μm/voxel. A) step-by-step zooming in scans with low magnification objectives of 0.4X and 4X, B) a cross-section view of the reconstructed volume acquired with a standard 40X objective, C) the corresponding cross-section with the 40X-P objective, D) a planar view of the reconstructed volume acquired with the standard 40X, and E) the corresponding planar view with the 40X-P objective.

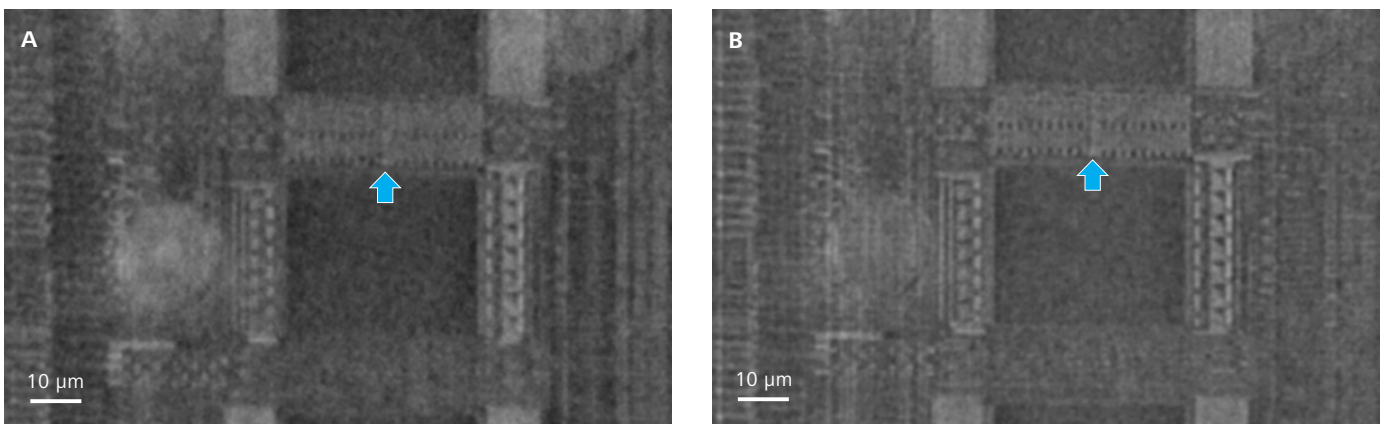


Figure 4 Resolution and contrast performance comparison of the 40X-P objective with a standard 40X objective on the DRAM package sample. The tomography was acquired at 0.49 μm/vox resolution. A) a planar virtual slice of the reconstructed volume acquired with a standard 40X objective, B) the corresponding view with the 40X-P objective.

EMIB packaging technique utilizes a small Si bridge to connect multiple dies. It is an alternative technique to 2.5D Si interposer packaging for its benefits on die placement flexibility and free of TSV process. An EMIB package was purchased through a commercial channel and the sample was not trimmed or prepared in the imaging work. Figure 5a shows the sample photo. A scan with 4X objective at $0.73\ \mu\text{m}/\text{vox}$ resolution was performed to precisely localize a micro-bump region for the following 40X scans (Figure 5b). Figure 5c-f shows the 3D microscopic images acquired at $0.32\ \mu\text{m}/\text{voxel}$ resolution with both 40X objective lenses. The virtual slice of the data acquired with the 40X-P objective shows the better resolution and contrast of the solder voids (Figure 5d) than with a standard 40X objective in Figure 5c. Even the smaller BOEL structures were resolved more clearly in the image acquired with the 40X-P objective. The example planar view in Figure 5f revealed the surface detail of metal traces, indicating the image obtained by the 40X-P objective delivers better resolution and contrast than the standard 40X objective.

To demonstrate that this new 40X-P detector can be efficiently used in X-ray failure analysis workflow, we utilized the deep learning reconstruction method reported previously [4-6] to improve the scan throughput while maintain the image quality. The standard Feldkamp-Davis-Kress (FDK) reconstruction provides accurate and fast reconstruction, but it is sensitive to photon starvation and resulting images are prone to noise and under-sampling artifacts. For example, a typical data acquisition with a 40X objective lens requires an overnight scan with the FDK reconstruction for high image quality. In a 3.5 hour scan with the 40X-P objective and FDK reconstruction, the detail of microbump and BOEL structures has not been clearly revealed due to high noise level (Figure 6a).

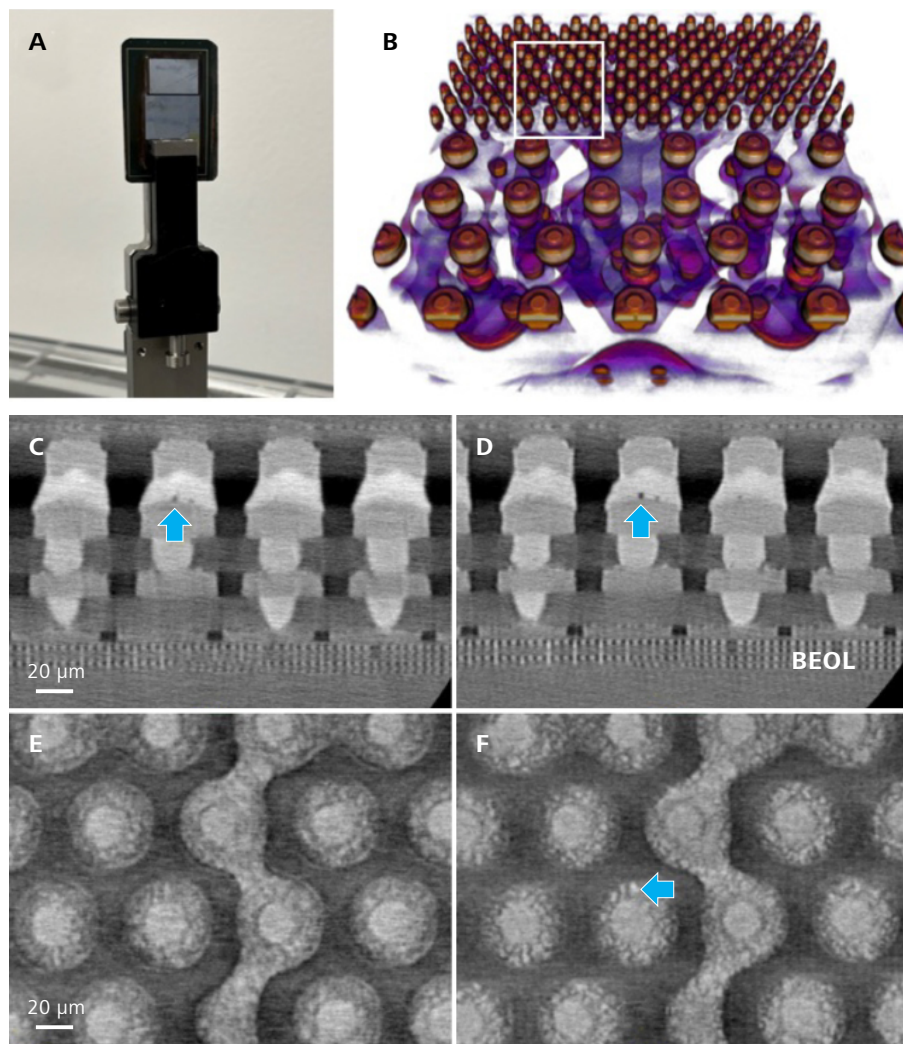


Figure 5 A comparison of the 40X-P objective to a standard 40X objective on the EMIB package sample. The images were acquired with both 40X objectives at $0.32\ \mu\text{m}/\text{vox}$ resolution. A) photo of the sample, B) the image was acquired with 4X at $0.73\ \mu\text{m}/\text{vox}$ for localizing 40X scans, C) a cross-section view of the reconstructed volume acquired with a standard 40X objective, D) the corresponding cross-section view with the 40X-P objective, E) a planar view of the reconstructed volume acquired with a standard 40X, and F) the corresponding cross-section view with the 40X-P objective.

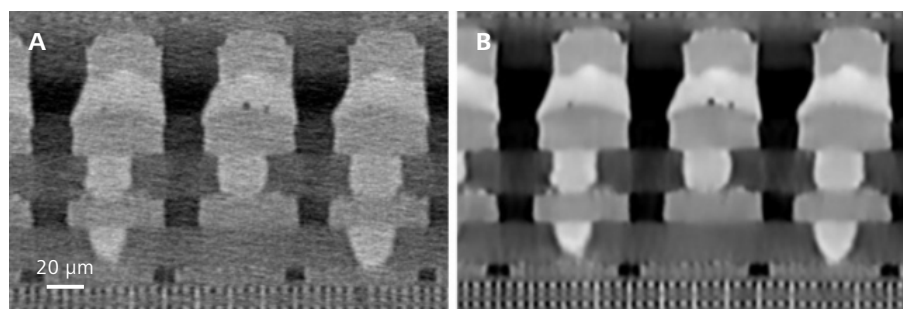


Figure 6 A comparative study of the deep learning reconstruction result to the standard FDK reconstruction. The tomography was acquired at $0.32\ \mu\text{m}/\text{vox}$ resolution with the 40X-P objective. A) a virtual slice from a 3.5 hour scan with the standard FDK reconstruction. B) the same virtual slice from a 3.5 hour scan with the deep learning reconstruction method.

By contrast, the 3.5 hour scan with the deep learning reconstruction clearly shows the improved image quality with the same scan time (Figure 6b). The result shows that the new 40X-P detector can be efficiently used for failure analysis workflows with unparalleled resolution and contrast.

Conclusion

The impacts of innovative packaging technologies have been seen across advanced semiconductor packages. The failure analysis community always carves for more effective and efficient non-destructive solutions for solving root cause analysis challenges in these complex packages. We demonstrated the breakthrough in resolution and contrast is enabled with a new scintillator material based X-ray detector in XRM. Because of its superior performance at higher energies over the traditional CsI scintillator based detector, it can be used in imaging high-density semiconductor packages. With the deep learning reconstruction workflow, the scan speed can be improved while maintaining the unprecedented resolution and contrast.

References

- [1] L. Mirkarimi, A. Gu, L. Hunter, G. Guevara, M. Huynh, R. Katkar, "X-ray Microscopy and Root Cause Analysis in Electronic Packaging", Proc 41st Int'l Symp for Testing and Failure Analysis, Portland, OR, Nov. 2015, pp. 430-435. doi: 10.31399/asm.cp.istfa2015p0430
- [2] S. M. Zulkifli, B. Zee, W. Qiu, A. Gu, "High-Res 3D X-ray Microscopy for Non-Destructive Failure Analysis of Chip-to-Chip Micro-bump Interconnects in Stacked Die Packages", IEEE 24th Int'l Symp on the Physical and Failure Analysis of Integrated Circuits (IPFA), Chengdu, China, Jul. 2017. doi:10.1109/IPFA.2017.8060111
- [3] A. Gu, J. Auyong, "3D Measurement Workflow for Packaging Development and Production Control Using High-Resolution 3D X-ray Microscope", 2018 IEEE 20th Electronics Packaging Tech Confer (EPTC), Singapore, Dec. 2018. doi:10.1109/EPTC.2018.8654390
- [4] M. Andrew, R. Sanapala, A. Andreyev, H. Bale, C. Hartfield, "Supercharging X-ray Microscopy Using Advanced Algorithms", Microscopy and Analysis, pp17, Nov/Dec 2020
- [5] A. Gu, A. Andreyev, M. Terada, B. Zee, S. M. Zulkifli, Y. Yang, "Accelerate Your 3D X-ray Failure Analysis by Deep Learning High Resolution Reconstruction Paper," Int'l Symp for Testing and Failure Analysis, No: istfa2021p0291, pp. 291-295, Phoenix, AZ, Dec 2021
- [6] A. Gu, M. Terada, H. Stegmann, T. Rodgers, C. Fu and Y. Yang, "From System to Package to Interconnect: An Artificial Intelligence Powered 3D X-ray Imaging Solution for Semiconductor Package Structural Analysis and Correlative Microscopic Failure Analysis," IPFA 2022, Singapore
- [7] C. Schmidt, S. Kelly, Y. Wang, S.T. Coyle, M. H. Shearer, "Novel sample preparation and High-Resolution X-ray tomography for Package FA," IEEE 24th Int'l Symp on the Physical and Failure Analysis of Integrated Circuits (IPFA), Chengdu, China, Jul. 2017
- [8] C. Schmidt, L. Lechner, I. DeWolf, S. W. Kim, E. Beyne, "Novel failure analysis techniques for 1.8 μm pitch wafer-to-wafer bonding," IEEE 68th Electronic Components and Technology Conference, San Diego, CA, May 2018.

Accelerate Your 3D X-ray Failure Analysis by Deep Learning High Resolution Reconstruction

Allen Gu, Andriy Andreyev, Masako Terada

Carl Zeiss Research Microscopy Solutions, 5300 Central Parkway, Dublin, CA 94568, USA

Bernice Zee, Syahirah Mohammad-Zulkifli

Advanced Micro Devices (Singapore) Pte Ltd, Device Analysis Lab 508 Chai Chee Lane, Singapore 469032

Yanjing Yang

Carl Zeiss X-ray Microscopy Applications, 50 Kaki Bukit Place, Singapore 415926

Abstract

Over the past decade, 3D X-ray has played a critical role in semiconductor package failure analysis (FA), primarily owing to its non-destructive nature and high resolution capability [1,2]. As novel complex IC packages soar in recent years [3,4], X-ray failure analysis faces increasing challenges in imaging new advanced packages because IC interconnects are more densely packed in larger platforms. It takes several hours to overnight to image fault regions at high resolution or crucial details of a defect remain undetected. A high-productivity X-ray solution is required to substantially speed up data acquisition while maintaining image quality. In this paper, we propose a new deep learning high-resolution reconstruction (DLHRR) method, capable of speeding up data acquisition by at least a factor of four through the implementation of pre-trained neural networks. We will demonstrate that DLHRR extracts signals from low-dose data more efficiently than the conventional Feldkamp-Davis-Kress (FDK) method, which is sensitive to noise and prone to the aliasing image artifacts. Several semiconductor packages and a commercial smartwatch battery module will be analyzed using the proposed technique. Up to 10x scan throughput improvement was demonstrated on a commercial IC package. Without the need of any additional X-ray beam-line hardware, the proposed method can provide a viable and affordable solution to turbocharge X-ray failure analysis.

Introduction

As the era of transistor scaling driven technology is coming to an end in the semiconductor industry, packaging innovation strives to continuously improve the performance and reliability of electronics products. The trend of 3D packaging and heterogenous integration has presented increasing challenges to existing FA techniques because of more complex multichip architectures and more miniaturized interconnects. The 3D X-ray workflow is known for enhancing FA success rates by its non-destructive and high-resolution imaging capabilities. However, its applications to advanced packages have become less effective due to increasing package complexity and density, together with the surging demand for non-destructive X-ray inspection.

A faster X-ray solution is required to substantially enhance the imaging efficiency so that the user does not have to compromise image quality and scan throughput in high resolution imaging.

Computed tomography (CT) image reconstruction, a necessary step in any 3D X-ray workflow, converts 2D projection images to a 3D volume. Most commercial CT systems utilize the traditional FDK algorithm for reconstruction. It can generate good quality images in a fast and reliable reconstruction process. In addition, it does not require as high computing power as other reconstruction methods such as iterative reconstruction. The FDK method, however, is sensitive to photon starvation and resulting images are prone to a variety of under-sampling artifacts. Consequently, a high number of projections, and/or long exposure time per projection are required for reducing image noise and artifacts. Long scans are necessary for high quality data acquisition. In this work, we will introduce and evaluate a new deep learning-based reconstruction method to overcome this hurdle.

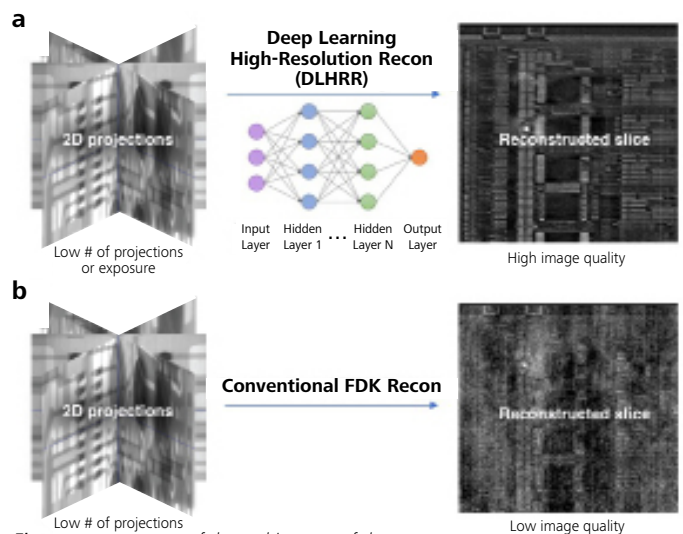


Figure 1. Comparison of the architecture of the proposed method (a) and its performance advantage over the conventional FDK method (b). With the same low number of projections, DLHRR generates higher quality images than the conventional FDK method.

Deep Learning High-resolution Reconstruction

Deep learning based convolutional neural networks have shown excellent performance in numerous computer vision tasks such as recognition, segmentation, resolution improvement, and denoising [5-8]. However, the reported methods are not directly useful to X-ray microscopy, where an actual 3D image has to be reconstructed from a set of 2D X-ray projections, in which the corrections for source spectrum, photon statistics, sample drifts and X-ray scattering are required to maintain the highest image resolution and quality.

The new convolutional neural network method is based on the “noise2noise” model and approach [9] with the ZEISS proprietary cost function and training data preparation protocol available under ZEISS DeepRecon Pro. The network proposed and evaluated in this work (Fig. 1) is more suitable for high-resolution image reconstruction, because it addresses image quality degradation in the scenario of low pixel counts or insufficient number of projections [10]. The training input is a set of low number of projections with high-noise pixels, and the training target is an image created from a high number of projections with low-noise pixels, which serves as the “ground truth” data.

The training of the network is done in a manner that it is applicable to the desired X-ray microscope data acquisition settings and a given sample class. The model will need to be retrained if such parameters change. However, the network is quite lightweight and can be re-trained within 3 hours on a relatively mid-range professional workstation (Dell Precision 7920) utilizing two professional GPUs totaling 48 GB of video RAM. Once the network is trained, it can be applied to all the tomographic data that belongs to the same class and the reconstruction itself takes less than 5 minutes for a 1000^3 voxels image volume. We intentionally minimized the number of parameters to be optimized to just one that controls the noise level dictated by the desired total acquisition scan time. It works especially well when the imaging task consists of several samples or ROIs that need to be imaged in the same or similar manner, since every subsequent sample/ROI does not require retraining of the network. Given the simplicity of the training process and the comparatively short training duration that is of the same order of magnitude as iterative reconstruction, we foresee that DLHRR will be used on unique samples as well.

Since the applicability of the network is narrowed to a strict sample class and acquisition conditions, the network can be trained on as little as one tomography. There are also no strict requirements towards the training data, other than the sample needing to be well represented with all characteristic features in the field-of-view. It is worth noting that even a single tomographic acquisition is three dimensional in nature, containing hundreds or thousands of 2D images.

This provides the network with enough training data. Furthermore, the training data are augmented during the training process to account for potential variations in sample and data acquisition conditions. Overall, the images reconstructed by the DLHRR method routinely result in better quality than the FDK-reconstructed images, in which the critical structural information is frequently lost due to the under-sampling noise and artifacts.

Results

In our first case study, 3D X-ray data was acquired at $0.7 \mu\text{m}/\text{vox}$ resolution on a $50 \times 50 \text{ mm}$ AMD HBM- μbump 2.5D package (Fig. 2a). The fault region was μbump joint cracks at the high-bandwidth memory stack and interposer interface, as shown in Fig. 2b. It is a 3D color-rendering image. With a typical setting of FDK reconstruction, 1,600 projections were acquired in a 9.6 hour tomography, revealing $\sim 1 \mu\text{m}$ thick bump cracks (Fig. 2c-d). The DLHRR slices in Fig. 2e-f) showed very similar image quality on the corresponding cracks with only 400 projections for a 2.4 hour scan. This case demonstrated that DLHRR successfully learned to differentiate signal and noise from the training data, achieving equivalent image quality without losing the visibility of the small features in a scan 4x faster than FDK.

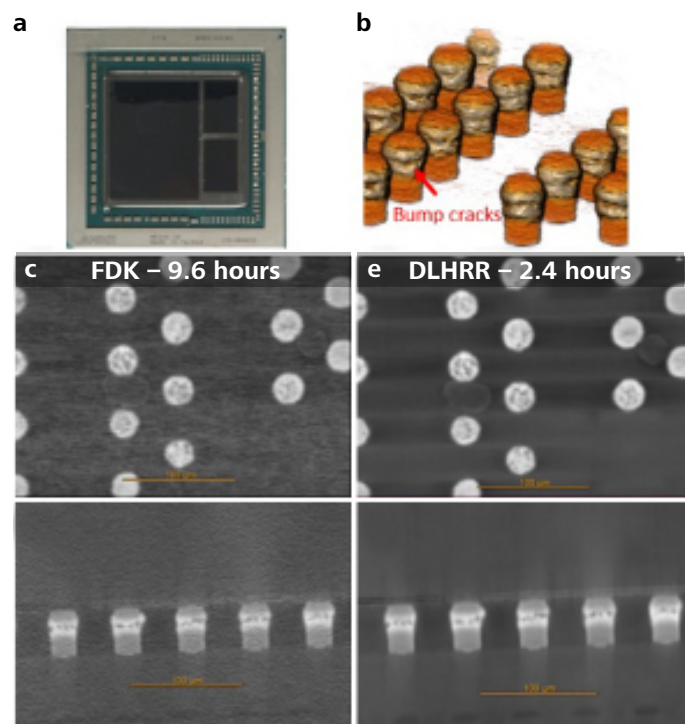


Figure 2 Comparison of the DLHRR results to FDK on a $50 \times 50 \text{ mm}$ AMD HBM- μbump package. a) sample, b) a 3D color-rendering image at $0.72 \mu\text{m}/\text{vox}$ resolution, c-d) virtual cross-section slices from the FDK 9.6 hour scan, e-f) virtual slices from the DLHRR 2.4 hour scan. c) and e) are the top-down views, and d) and f) are the cross-sectional views.

In the second case study, X-ray scans were obtained at $1.5\ \mu\text{m}/\text{vox}$ resolution on a commercial $10\times 10\ \text{mm}$ smartphone A8 package. Both FDK and DLHRR reconstruction methods were performed for comparison. Since there were no known electrical open or short failures in the test sample, we focused on solder ball and via voids, a common defect in IC packages. Fig. 3a) shows an example slice from the 6 hour scan reconstructed by FDK. The image quality is acceptable with this long scan. As the X-ray dose decreased by a factor of ten, the traditional FDK method showed its inefficiency to extract signal from the 0.6 hour scan (data not shown). By contrast, the slice from the same short scan but reconstructed by DLHRR maintained the high image quality – no image detail was lost (Fig. 3b).

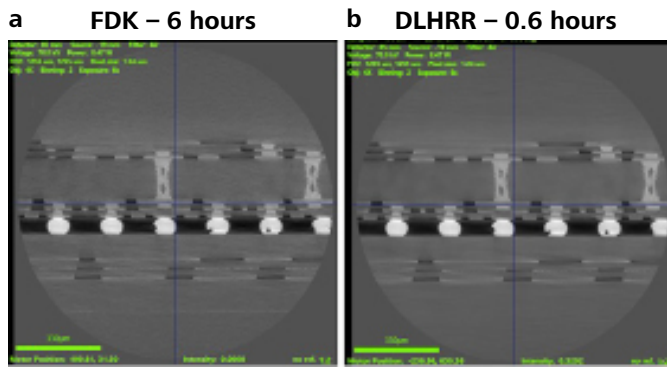


Figure 3 A comparison of the virtual slices extracted from a) the FDK 6 hour scan, b) the DLHRR 0.6 hour scan at $1.5\ \mu\text{m}/\text{vox}$ resolution on a smartphone A8 package.

Analysis time is critical in semiconductor package reliability testing because package structures may alter over the test cycles. To understand throughput improvement for 3D X-ray application in reliability testing, we acquired data on a 2.5D interposer package tested by using the JEDEC thermal cycle standard (Fig. 4a). The 4 hour and 1 hour scan results at $0.7\ \mu\text{m}/\text{vox}$ were reconstructed by both DLHRR and FDK methods for comparison. Fig.4b is the 3D color-rendering image from the FDK 4 hour scan, showing the defective bumps at the corner of the package. The virtual cross-sectional slice from FDK 4 hour (Fig. 4c) and DLHRR 1 hour (Fig. 4d) scans resulted in very comparable image quality, clearly visualizing $\sim 2\ \mu\text{m}$ cracks at C4 bumps, the byproduct of the thermal cycle. With the high-level noise in the FDK 1 hour data (not shown), the crack information may be misinterpreted. This case demonstrated that the DLHRR method was effective to reduce the scan time by a factor of four, compared with the standard FDK reconstruction.

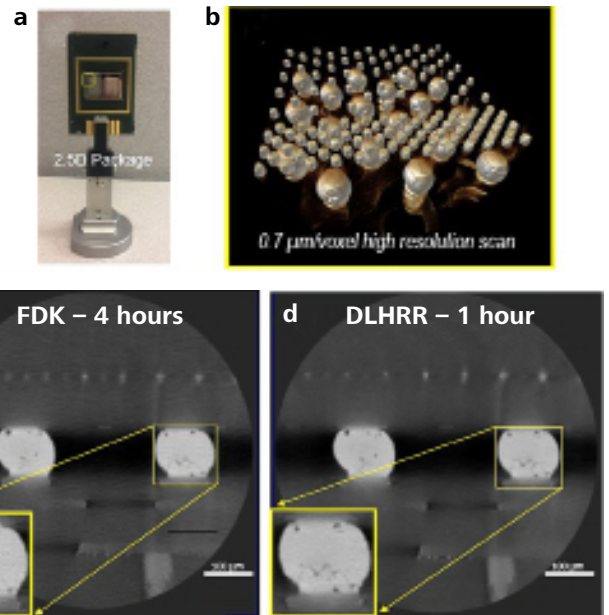


Figure 4 DLHRR results used in the reliability study of a $50\times 75\ \text{mm}$ 2.5D interposer package. a) sample, b) a 3D color-rendering image for the defective corner of the package, acquired at $0.7\ \mu\text{m}/\text{vox}$, c) a reconstructed slice by the FDK 4 hour scan, d) a reconstructed slice by the DLHRR 1 hour scan. The insets in c-d) are the digitally zoomed-in images on the cracked bump.

3D X-ray imaging and analysis are important in quality inspection and longevity study of lithium-ion batteries. A high-resolution interior tomography on a battery sample can take ~ 24 hours with the traditional FDK reconstruction. To test the scan throughput improvement by the new DLHRR method, we acquired 3D X-ray data on a commercial smartwatch battery module, which were later reconstructed by these two methods for a comparative study (Fig. 5). The baseline data from the FDK 24 hour scan are shown in Fig. 5a-b). When reducing the number of projections by a factor of four (Fig. 5c), the FDK slice showed a high level of noise, which shadowed the visibility of the polymer separator, a key structure relevant to battery performance. The low data quality resulted from under-sampling noise and artifacts in the FDK reconstruction, which would make it difficult for subsequent segmentation and quantification. By contrast, the DLHRR slice (Fig. 5d) showed clear particle boundary definitions even at the reduced scan time at 6 hours. It was found that the contrast-to-noise ratio from the DLHRR 6 hour scan is even higher than the FDK 24 hour scan. This case further demonstrated the effectiveness of the new DLHRR reconstruction method to reduce the data acquisition time by a factor of four.

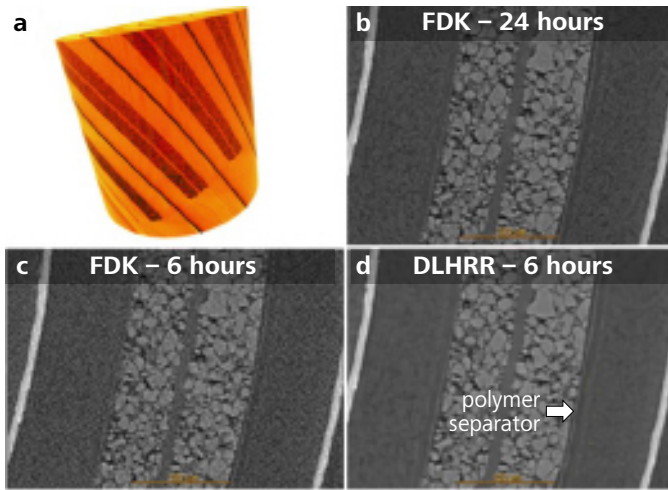


Figure 5 A comparative study of the DLHRR results to FDK on a commercial smartwatch battery module. The tomography was acquired at $0.53 \mu\text{m}/\text{vox}$ resolution. a) a 3D color-rendering image from the FDK 24 hour scan, b) a virtual slice from the FDK 24 hour scan, c) a virtual slice from the FDK 6 hour scan, d) a virtual slice from the DLHRR 6 hour scan.

So far we have demonstrated that the DLHRR method can be used for reducing scan time significantly on several cases. It can also be used for improving image quality in a same scan time setting. 3D X-ray data were acquired at $1 \mu\text{m}/\text{vox}$ resolution on a commercial 4-High DRAM package (Fig. 6). The sample was chosen because it has about $2 \mu\text{m}$ thin metal lines on the top of dies, a good target for image quality assessment. With FDK reconstruction, 400 projections were acquired in a 30 minute tomography. The resulting top-down view and cross-sectional views are showed in Fig. 6 a-b. The metal lines however were largely smeared due to the high level of noise generated by the traditional reconstruction method in the low X-ray dose tomographic scan (Fig. 6b). The small structure may be overlooked due to the low image quality. Longer scans are generally required to retain this small feature. With the DLHRR method, the visibility of the same metal lines was largely enhanced (Fig. 6d) even in the short scan data. During the network training process, the machine has learned to recognize the small feature and the surrounding noise. Compared with the high level of noise in Fig. 6a, the DLHRR results show higher contrast-to-noise ratio in the top-down view (Fig. 6c). This case demonstrated the effectiveness of the new DLHRR reconstruction method to improve image quality in the same scan time, especially for short scans. As modern advanced packages become more complex, defects and failures are more difficult to image and characterize. Highest image quality with shortest scan time is always preferred in 3D X-ray failure analysis workflows to enhance the success rate of root cause analyses.

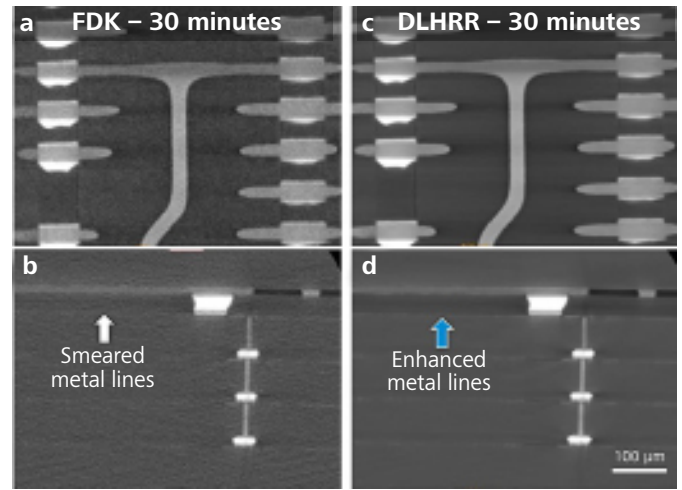


Figure 6 With the same scan time, the DLHRR results in c-d) show superior image quality over the FDK results in a-b). The data was acquired on a commercial $\mu\text{bump-TSV}$ DRAM sample at $1 \mu\text{m}/\text{vox}$ resolution. The blue arrow in d) shows an enhanced contrast-to-noise ratio on the metal lines, which were smeared in the FDK result. a) and c) are top-down views. b) and d) are cross-sectional views.

3D volume stitching plays an important role in FA fault isolation, intellectual property intelligence and reverse engineering applications. The benefit is to achieve higher resolution for a field of view (FOV) through multiple-volume stitching, overcoming the detector size limitation. However, the total scan time is long because of the multi-volume data acquisition. The DLHRR method can elevate the scan efficiency without losing image quality because the time reduction for a single volume scan can be applied to other volumes without the need of an additional network training. The test sample was the entire accelerator/gyroscope package, as indicated by the red box in Fig. 7a, of a commercial smartphone mother board. We acquired 3×3 volumes with $1.6 \mu\text{m}/\text{voxel}$ resolution for each volume. With a typical FDK reconstruction setting, it took 100 minutes for each volume. The nine volumes took the total of 900 minutes and the stitched data are shown in Fig. 7 b-c. With the DLHRR reconstruction method, only 25 minutes per scan was required. As shown in Fig. 7e, the 25 minutes scan and DLHRR reconstruction generated excellent image quality. By contrast, the result from a 25 minutes scan and FDK reconstruction showed a high level of noise and rich streak artifacts (Fig. 7d), which may cause a failure of stitching. The visibility of the Si structure was overshadowed by the noise. In this case, the DLHRR method succeeded to reduce the total scan time to 225 minutes in the data acquisition of all the stitched volumes, which requires 900 minutes scan with the traditional FDK method. The trained network model based on the center volume was successfully applied on all other volumes. We demonstrated that the DLHRR can be used to improve the image resolution over larger FOVs through more efficient multiple-volume data acquisition and stitching.

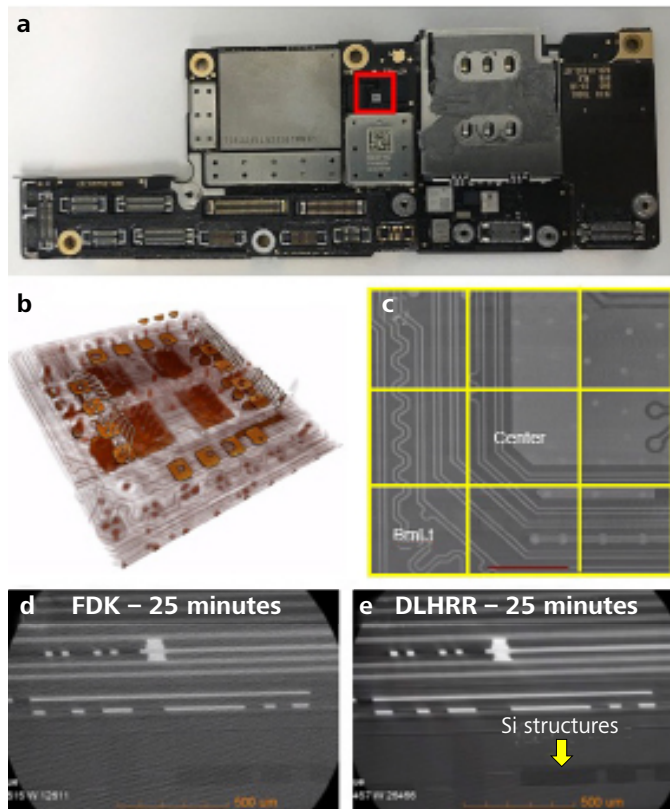


Figure 7 DLHRR was used in a test of multiple volumes stitching. *a)* an accelerator/gyroscope package in a commercial smartphone motherboard. *b)* 3x3 stitched volumes. *c)* a virtual cross-section of the stitched volume from the FDK reconstruction. *d)* a virtual slice from the FDK 25 minute scan. *e)* a corresponding slice from the DLHRR 25 minute scan. Both scans were acquired at 1.6 $\mu\text{m}/\text{voxel}$ resolution.

Acknowledgements

We thank Dr. Lars Omlor, Dr. Matthew Andrew, and Dr. Christoph Hilmar Graf vom Hagen, Carl Zeiss X-ray Microscopy, Dublin, CA, USA, for the DLHRR algorithm development, and instrumental discussions on its applications.

© [2021] Advanced Micro Devices, Inc. All rights reserved. AMD, the AMD Arrow logo, and combinations thereof are trademarks of Advanced Micro Devices, Inc. Other product names used in this publication are for identification purposes only and may be trademarks of their respective companies.

Reference

- [1] L. Mirkarimi, A. Gu, L. Hunter, G. Guevara, M. Huynh, R. Katkar, "X-ray Microscopy and Root Cause Analysis in Electronic Packaging", Proc 41st Int'l Symp for Testing and Failure Analysis, Portland, OR, Nov. 2015, pp. 430-435. doi: 10.31399/asm.cp.istfa2015p0430
- [2] S. M. Zulkifli, B. Zee, W. Qiu, A. Gu, "High-Res 3D X-ray Microscopy for Non-Destructive Failure Analysis of Chip-to-Chip Micro-bump Interconnects in Stacked Die Packages", IEEE 24th Int'l Symp on the Physical and Failure Analysis of Integrated Circuits (IPFA), Chengdu, China, Jul. 2017. doi:10.1109/IPFA.2017.8060111
- [3] T. Gregorich, M. Terada, C. Hartfield, A. Gu and J. Vardaman, "Non-destructive Characterization of Application Processor Panel Level Package Used in Galaxy Smartwatch", 2019 Int'l Wafer Level Packaging Confer., San Jose, CA, Oct. 2019, pp. 1-7. doi: 10.23919/IWLPC.2019.8914126
- [4] A. Gu, J. Auyoong, "3D Measurement Workflow for Packaging Development and Production Control Using High-Resolution 3D X-ray Microscope", 2018 IEEE 20th Electronics Packaging Tech Confer (EPTC), Singapore, Dec. 2018. doi:10.1109/EPTC.2018.8654390
- [5] K. Simonyan and A. Zisserman, "Very Deep Convolutional Networks for Large-Scale Image Recognition", Int'l Confer. on Learning Representations, 2015, arXiv:1409.1556
- [6] V. Badrinarayanan, A. Kendall and R. Cipolla, "SegNet: A Deep Convolutional Encoder-Decoder Architecture for Image Segmentation", IEEE Transactions on Pattern Analysis and Machine Intelligence, vol. 39, issue 12, 2017
- [7] C. Ledig, L. Theis, F. Huszar, J. Caballero, A. Cunningham, A. Acosta, A. Aitken, A. Tejani, J. Totz, Z. Wang and W. Shi, "Photo-Realistic Single Image Super-resolution Using a Generative Adversarial Network" in Computer Vision and Pattern Recognition, 2017
- [8] K. Zhang, W. Zuo, Y. Chen, D. Meng and L. Zhang, "Beyond a Gaussian Denoiser: Residual Learning of Deep CNN for Image Denoising", IEEE Transactions on Image Processing, vol. 26, issue, 7, 2017
- [9] J. Lehtinen, J. Munkberg, J. Hasselgren, S. Laine, T. Karras, M. Aittala, and T. Aila, "Noise2Noise: Learning Image Restoration without Clean Data," 35th Int. Conf. Mach. Learn. ICML 2018 7 (2018).
- [10] M. Andrew, R. Sanapala, A. Andreyev, H. Bale, C. Hartfield, "Supercharging X-ray Microscopy Using Advanced Algorithms", Microscopy and Analysis, pp17, Nov/Dec 2020

Conclusion

The impacts of artificial intelligence technology have been seen across most industrial segments and commercial services such as transportation, healthcare, education, on-line shopping, finance and many more. This technological development provides a golden opportunity for the electronics failure analysis society to enable capability improvement and revolution. In this report, we demonstrated a deep learning based high-resolution reconstruction technique which can be used to substantially shorten X-ray failure analysis workflows. The throughput improvement by a factor of four or ten was demonstrated for several semiconductor package examples. Since the network can be trained on as little as one tomography dataset, its application range is limited to the sample class and acquisition condition specified by that training dataset. Network applicability to broad sample classes can be improved with further development. It is also possible to extend 3D X-ray applications to other high-productivity areas such as fault screening and isolation, package construction analysis, and even in-line inspection and metrology.

A Deep Learning Reconstruction Technique and Workflow to Enhance 3D X-ray Imaging Resolution and Speed for Electronics Package Failure Analysis

Allen Gu, Andriy Andreyev, Masako Terada

Carl Zeiss Research Microscopy Solutions, 5300 Central Parkway, Dublin, CA 94568, USA

Thomas Rodgers

Carl Zeiss Microscopy GmbH, Rudolf Eber Str. 2, BG 41/1, 73447 Oberkochen, Germany

Vignesh Viswanathan

Carl Zeiss Pte. Ltd., 80 Bendemeer Road, #10-01, Singapore 339949

Abstract

3D X-ray imaging plays an important role in package level failure analysis. Like most other microscopies, X-ray microscopes (XRM) generally have field of view (FOV) limits for high-resolution imaging. As precise fault isolation becomes more challenging in large and complex IC packages, acquiring numerous high-resolution images to search for defects in a large FOV is required. For example, if a suspect fault region is 785 mm³ in a cylinder with 10 mm in diameter and 10mm in height, more than 125 high-resolution scans with 6.28 mm³ each are required to cover the volume. This significantly diminishes XRM imaging throughput. In this report, we propose a new deep learning reconstruction method to address the issue of achieving high-resolution at large FOVs. This AI powered technique and workflow can be used to restore the resolution from a large FOV scan.

Introduction

3D XRM imaging technique has been widely adopted to failure analysis and characterization of electronics systems and packages. With its non-destructive and high resolution imaging capability, deeply buried defects can be visualized prior to physical failure analysis (PFA). The X-ray microscopic technique, however, faces a challenge in imaging new IC packages where more densely packed interconnects are built in larger platforms. Because of the difficulty to pinpoint defect locations, it is often required to scan a large FOV with high resolution and speed, leading to the time-consuming and sometimes impractical X-ray imaging process.

In this paper, we introduce a novel deep learning based reconstruction method, capable of learning the point spread function (PSF) of low resolution data by training on a pair of high and low resolution data. By operationalizing the trained network model, low resolution data is transformed to high resolution data through an inference process.

We will demonstrate on several IC packages that the proposed workflow can be utilized in fault isolation for a large area, in which standard XRM has not been practically possible due to the trade-off of image resolution and FOV, a fundamental limit for most microscopes.

Method

A conventional approach to improve image sharpness is to deconvolve the estimated PSF of the imaging system from actual tomographic images, e.g. using Richardson-Lucy deconvolution [1-2]. However, the accurate derivation of PSF requires the analytical modelling of data acquisition geometry, which may not reflect actual measurement conditions of a given sample. Additionally, the deconvolution process is computationally expensive, often leading to high levels of noise and artefacts. In this paper, we propose a novel approach to recover image resolution where the deconvolution step is replaced with applying a convolutional neural network trained specifically on the spatially registered low-to-high resolution feature map (Figure 1). The workflow starts with a spatial registration of multi-resolution data pair acquired for a sample.

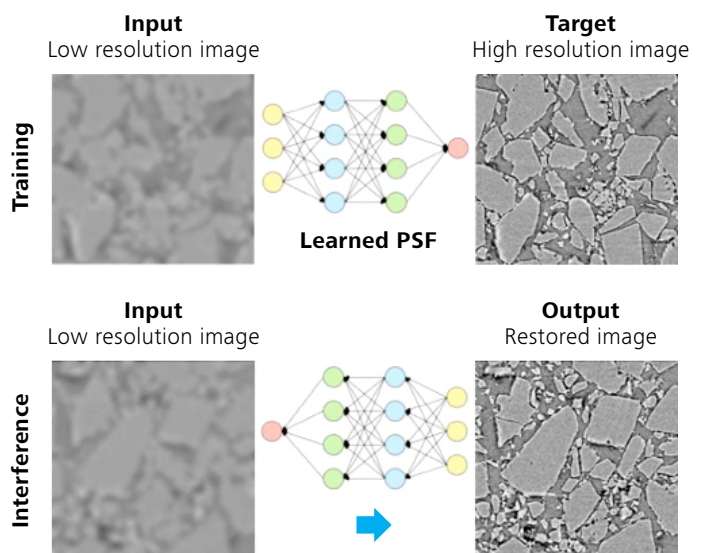


Figure 1 Schematics of deep learning reconstruction method to restore image resolution from the low-resolution image input.

A network is then trained to remove the PSF effects at the low-resolution data. The recovery of image sharpness and removal of the uncorrelated image noise and artefacts are achieved because the network effectively learns the coupled effects of a finite PSF and partial volume artifacts.

In our first case study, a smartphone board with an A12 bionic System on Chip (SoC) package was commercially purchased (Figure 2). The sample was tested under a JEDEC reliability test standard with 1,000 temperature cycles to create solder cracks. In the second case study, an A14 SoC package was acquired through a commercial channel. We focused the deep learning reconstruction study on the small redistribution layers and PCB metal traces. Training data pairs can be easily obtained with an XRM instrument because it is capable of acquiring multi-level resolution data.

Results and Discussions

The low-resolution data at $10\ \mu\text{m}/\text{voxel}$ (Figure 2b-c) and the high-resolution data at $2.1\ \mu\text{m}/\text{voxel}$ were acquired within the volume of the low-resolution data (Figure 2b). First, these two datasets were spatially registered by using the reported methods [3-4] with 9-degree freedom to absorb small offsets resulting from imperfect machine alignments and possible sample drifts. Second, the resolution recovery network was trained using the modified image-to-image regression techniques [5-6] with loss functions, network structures and data augmentations tailored to the 3D tomographies. Finally, as a network model training is complete, the inference step was performed across the entire LFOV image or specific regions of interest, resulting in the recovered high-resolution image (Figure 2d).

Figure 2d shows the example slice of the restored image. In contrast to the original low-resolution image in Figure 2c, the deep learning recovered image reveals more details of the bump cracks, while the same defect looked more ambiguous and less conclusive in Figure 2c because of the resolution limit. Additionally, the beam hardening artifacts associated with the wire bonding are significantly reduced in the deep learning recovered image. The volume of the original low-resolution image is $\sim 14,130\ \text{mm}^3$ and the volume of the high-resolution image is $\sim 131\ \text{mm}^3$. The calculated volume gain is 108, the minimum number of scans without considering the overlapping regions would be required to achieve the volume and resolution of the deep learning recovered image.

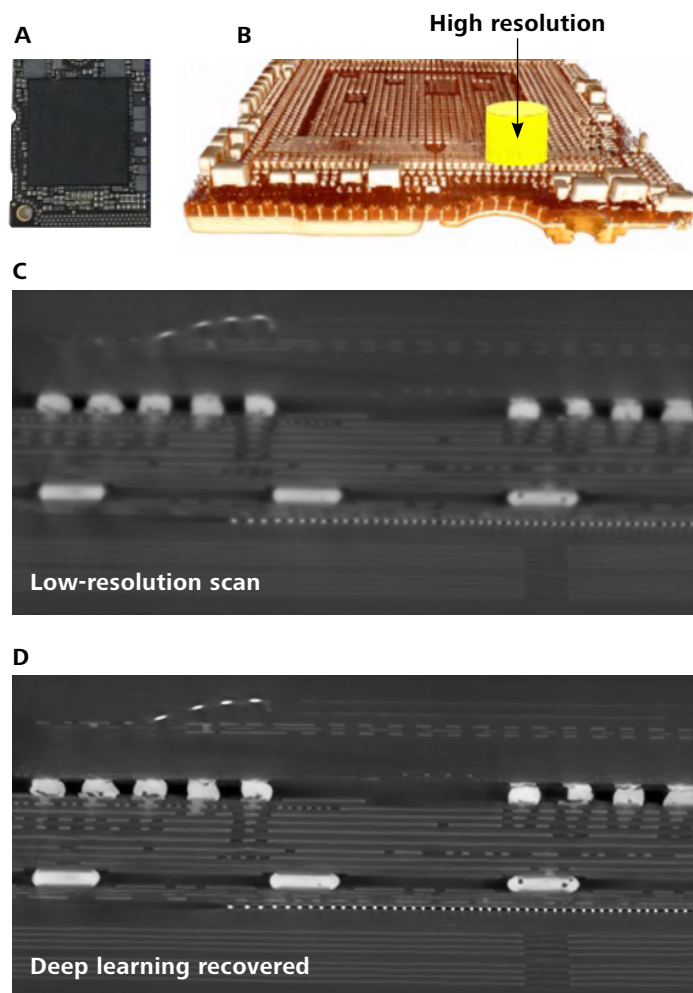


Figure 2 A) A12 SoC package test vehicle; B) 3D color-rendered image of the low-resolution scan; C) a virtual cross-section of the acquired low-resolution image; D) the same virtual slice from the low-resolution scan but restored with the deep learning reconstruction method.

A pair of low-resolution and high-resolution data was acquired with a 4X objective lens at $4.5\ \mu\text{m}/\text{voxel}$ and $1.5\ \mu\text{m}/\text{voxel}$ respectively. The deep learning network was generated through training these two data. The reconstructed slice in Figure 3b shows the image recovered by the deep learning reconstruction, revealing more microscopic details on the redistribution layers and PCB metal traces, compared with the original low-resolution scan in Figure 3a. This example demonstrates that the deep learning reconstruction can work on the data with small structures.

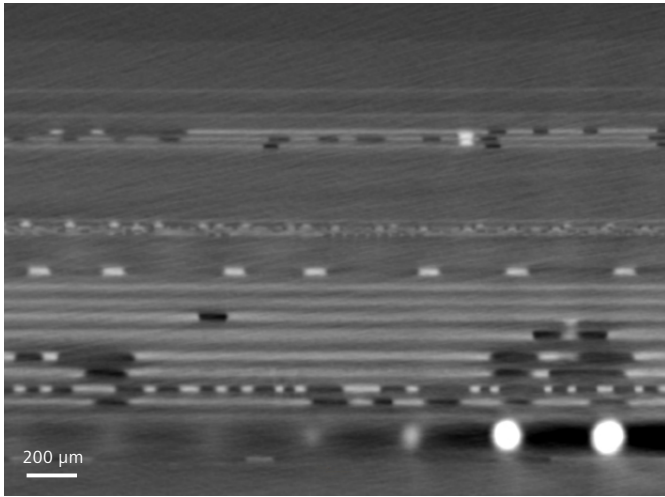
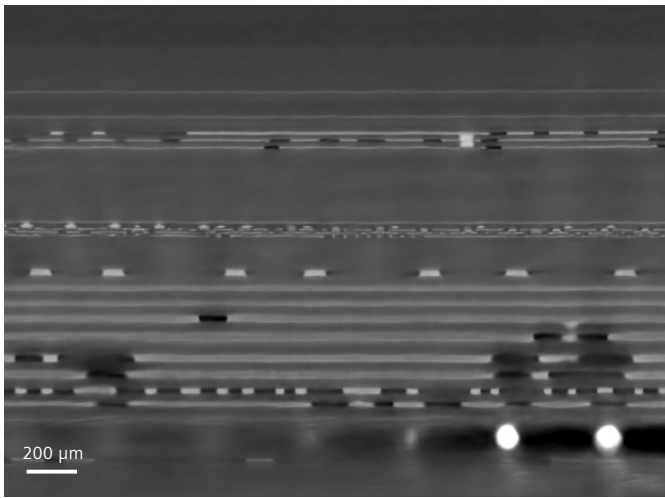
C**D**

Figure 3 A) the low-resolution image at $4.5 \mu\text{m}/\text{voxel}$; B) the image recovered by the deep learning reconstruction.

Conclusions

As new package architectures trend towards increased 3D packaging and heterogeneous integration, the traditional fault isolation techniques, such as acoustic microscopy, lock-in thermography, and time delay reflectometry, become less effective to localize the true fault regions. The deep learning powered X-ray imaging technique proposed here can extend to fault isolation applications, which are traditionally impractical, because it can be used to recover the resolution of a large volume.

References

- [1] W. H. Richardson, "Bayesian-Based Iterative Method of Image Restoration". *JOSA*. 62 (1): 55–59, 1972. doi:10.1364/JOSA.62.000055.
- [2] L. B. Lucy, "An iterative technique for the rectification of observed distributions". *Astronomical Journal*. 79 (6): 745–754, 1974. doi:10.1086/111605.
- [3] D. Mattes, D. R. Haynor, H. Vesselle, T. K. Lewellyn, and W. Eubank, "Nonrigid multimodality image registration," *Proc. SPIE Med. Imaging*, vol. 4322, 2001.
- [4] D. C. Liu and J. Nocedal, "On the limited memory BFGS method for large scale optimization," *Math. Program.*, vol. 45, no. 1–3, 1989, doi: 10.1007/BF01589116
- [5] J. Lehtinen et al., "Noise2Noise: Learning image restoration without clean data," in 35th International Conference on Machine Learning, ICML 2018, 2018, vol. 7.
- [6] M. Andrew, A. Andreyev, F. Yang, M. Terada, A. Gu, and R. White "Fully automated deep learning-based resolution recovery", *Proc. SPIE 12242, Developments in X-Ray Tomography XIV*, 122420M, 3 October 2022, <https://doi.org/10.1117/>



microscopy@zeiss.com
www.zeiss.com/semiconductor-microscopy